The Astrophysical Journal, 652:1475–1493, 2006 December 1
© 2006. The American Astronomical Society. All rights reserved. Printed in U.S.A.

PARTICLE ACCELERATOR IN PULSAR MAGNETOSPHERES: SUPER-GOLDREICH-JULIAN CURRENT WITH ION EMISSION FROM THE NEUTRON STAR SURFACE

Kouichi Hirotani[1]
ASIAA/National Tsing Hua University-TIARA, P.O. Box 23-141, Taipei, Taiwan; hirotani@tiara.sinica.edu.tw
Received 2006 April 2; accepted 2006 August 1

ABSTRACT

We investigate the self-consistent electrodynamic structure of a particle accelerator in the Crab pulsar magnetosphere on the two-dimensional poloidal plane, solving the Poisson equation for the electrostatic potential together with the Boltzmann equations for electrons, positrons, and γ-rays. If the transfield thickness of the gap is thin, the created current density becomes sub-Goldreich-Julian, giving the traditional outer-gap solution but with negligible γ-ray luminosity. As the thickness increases, the created current increases to become super-Goldreich-Julian, giving a new gap solution with substantially screened acceleration electric field in the inner part. In this case, the gap extends toward the neutron star with a small-amplitude positive acceleration field, extracting ions from the stellar surface as a space-charge-limited flow. The acceleration field is highly unscreened in the outer magnetosphere, resulting in a γ-ray spectral shape that is consistent with the observations.

Subject headings: gamma rays: observations — gamma rays: theory — magnetic fields — methods: numerical — pulsars: individual (Crab)

Online material: color figures

1. INTRODUCTION

The Energetic Gamma-Ray Experiment Telescope (EGRET) aboard the *Compton Gamma-Ray Observatory* has detected pulsed signals from at least six rotation-powered pulsars (e.g., for the Crab pulsar; Nolan et al. 1993; Fierro et al. 1998). Since interpreting γ-rays should be less ambiguous compared with reprocessed, nonthermal X-rays, the γ-ray pulsations observed from these objects are particularly important as a direct signature of basic nonthermal processes in pulsar magnetospheres, and potentially should help to discriminate among different emission models.

The pulsar magnetosphere can be divided into two zones (Fig. 1): the closed zone filled with a dense plasma corotating with the star, and the open zone in which plasma flows along the open field lines to escape through the light cylinder. The last open field lines form the border of the open magnetic field line bundle. In all the pulsar emission models, particle acceleration and the resulting photon emissions take place within this open zone.

On the spinning neutron star surface, an electromotive force, EMF $\approx \Omega^2 B_* r_*^3/c^2 \approx 10^{16.5}$ V, is exerted from the magnetic pole to the rim of the polar cap. In this paper, we assume that both the spin and magnetic axes reside in the same hemisphere; that is, $\boldsymbol{\Omega} \cdot \boldsymbol{\mu} > 0$, where $\boldsymbol{\Omega}$ represents the rotation vector and $\boldsymbol{\mu}$ the stellar magnetic moment vector. This strong EMF causes the magnetospheric currents that flow outward in the lower latitudes and inward near the magnetic axis (Fig. 2, *left*). The return current is formed at large distances where Poynting flux is converted into kinetic energy of particles or dissipated (Shibata 1997).

Attempts to model the particle accelerator have traditionally concentrated on two scenarios: polar-cap models with emission altitudes of $\sim 10^4$ cm to several neutron star radii over a pulsar polar cap surface (Harding et al. 1978; Daugherty & Harding 1982, 1996; Dermer & Sturner 1994; Sturner et al. 1995), and outer-gap models with acceleration occurring in the open zone located near the light cylinder (Cheng et al. 1986a, 1986b, hereafter CHR86a, CHR86b; Chiang & Romani 1992, 1994; Romani & Yadigaroglu 1995). Both models predict that electrons and positrons are accelerated in a charge depletion region, a potential gap, by the electric field along the magnetic field lines to radiate high-energy γ-rays via the curvature and inverse Compton (IC) processes.

In the outer magnetosphere picture of Romani (1996), he estimated the evolution of high-energy flux efficiencies and beaming fractions to discuss the detection statistics, by considering how pair creation on thermal surface flux can limit the acceleration zones. Subsequently, Cheng et al. (2000, hereafter CRZ00) developed a three-dimensional outer magnetospheric gap model, self-consistently limiting the gap size by pair creation from collisions of thermal photons from the polar cap that is heated by the bombardment of gap-accelerated charged particles. The outer gap models of these two groups have been successful in explaining the observed light curves, particularly in reproducing the wide separation of the two peaks commonly observed from γ-ray pulsars (Kanbach 1999; Thompson 2001), without invoking a very small inclination angle. In these outer gap models, they consider that the gap extends from the null surface, where the Goldreich-Julian (GJ) charge density vanishes, to the light cylinder, beyond which the velocity of a corotating plasma would exceed the velocity of light, adopting the vacuum solution of the Poisson equation for the electrostatic potential (CHR86a).

However, it was analytically demonstrated by Hirotani et al. (2003, hereafter HHS03) that an active gap, which must be nonvacuum, possesses a qualitatively different properties from the vacuum solution discussed in traditional outer-gap models. For example, the gap inner boundary shifts toward the star as the created current increases and at last touch the star if the created current exceeds the GJ value at the surface. Therefore, to understand the particle accelerator, which extends from the stellar surface to the outer magnetosphere, we have to merge the outer-gap and polar-cap models, which have been separately considered so far.

In traditional polar-cap models, the energetics and pair cascade spectrum have had success in reproducing the observations. However, the predicted beam size of radiation emitted near the stellar surface is too small to produce the wide pulse profiles that are

[1] Postal address: TIARA, Department of Physics, National Tsing Hua University, 101, Section 2, Kuang Fu Road, Hsinchu 300, Taiwan.

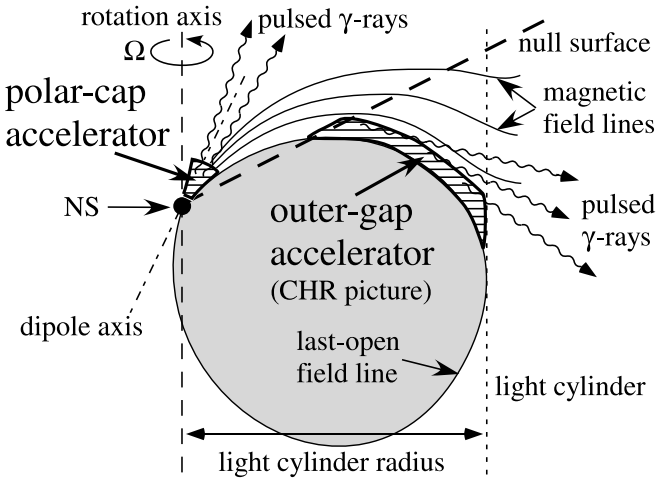


FIG. 1.—Schematic figure (side view) of the two representative accelerator models. The small filled circle represents the neutron star.

observed from high-energy pulsars. Seeking the possibility of a wide hollow cone of high-energy radiation due to the flaring of field lines, Arons (1983) first examined the particle acceleration at the high altitudes along the last open field line. This type of accelerator, or the slot gap, forms because the pair formation front (PFF), which screens the accelerating electric field, $E_\parallel$, in a width comparable to the neutron star radius, occurs at increasingly higher altitude as the magnetic colatitude approaches the edge of the open field region (Arons & Scharlemann 1979). Muslimov & Harding (2003, hereafter MH03) extended this argument by including two new features: acceleration due to spacetime dragging, and the additional decrease of $E_\parallel$ at the edge of the gap due to the narrowness of the slot gap. Moreover, Muslimov & Harding (2004a, 2004b, hereafter MH04a, MH04b) matched the high-altitude slot gap solution for $E_\parallel$ to the solution obtained at lower altitudes (MH03), and found that the residual $E_\parallel$ is small and constant, but still large enough at all altitudes to maintain the energies of electrons, which are extracted from the star, above 5 TeV.

It is noteworthy that the polar-slot gap model proposed by MH04a and MH04b is an extension of the polar-cap model into the outer magnetosphere, assuming that the plasma flowing in the gap consists of only one sign of charges. This assumption is self-consistently satisfied in their model, because pair creation in the extended slot gap occurs at a reduced rate and the pair cascade due to inward-migrating particles does not take place. In the polar-slot gap model, the completely charge-separated, space-charge-limited flow (SCLF) leads to a negative $E_\parallel$ for $\mathbf{\Omega} \cdot \boldsymbol{\mu} > 0$. However, we should note here that the electric current induced by the negative $E_\parallel$ (Fig. 2, *right*) contradicts with the global current patterns (Fig. 2, *left*), which is derived by the EMF exerted on the spinning neutron-star surface, if the gap is located near the last-open field line. (Note that the return current sheet is not assumed on the last-open field line in the slot gap model.)

On these grounds, we are motivated by the need to contrive an accelerator model that predicts a consistent current direction with the global requirement. To this aim, it is straightforward to extend recent outer-gap models, which predict opposite $E_\parallel$ to polar-cap models, into the inner magnetosphere. Extending the one-dimensional analysis along the field lines in several outer-gap models (Hirotani & Shibata 1999a, 1999b, 1999c; HHS03), Takata et al. (2004, hereafter TSH04) and Takata et al. (2006, hereafter TSHC06) solved the Poisson equation for the electrostatic potential on the two-dimensional poloidal plane, and revealed that the gap inner boundary is located inside of the null surface owing to the pair creation within the gap, assuming that the particle motion immediately saturates in the balance between electric and radiation-reaction forces.

In the present paper, we extend TSH04 and TSHC06 by solving the particle energy distribution explicitly, and by considering a super-GJ current solution with ion emission from the neutron star surface. In § 2, we formulate the basic equations and boundary conditions. We then apply it to the Crab pulsar in § 3 and compare the solution with MH04 in § 4.

2. GAP ELECTRODYNAMICS

In this section, we formulate the basic equations to describe the particle accelerator, extending the method first proposed by Beskin et al. (1992) for black hole magnetospheres.

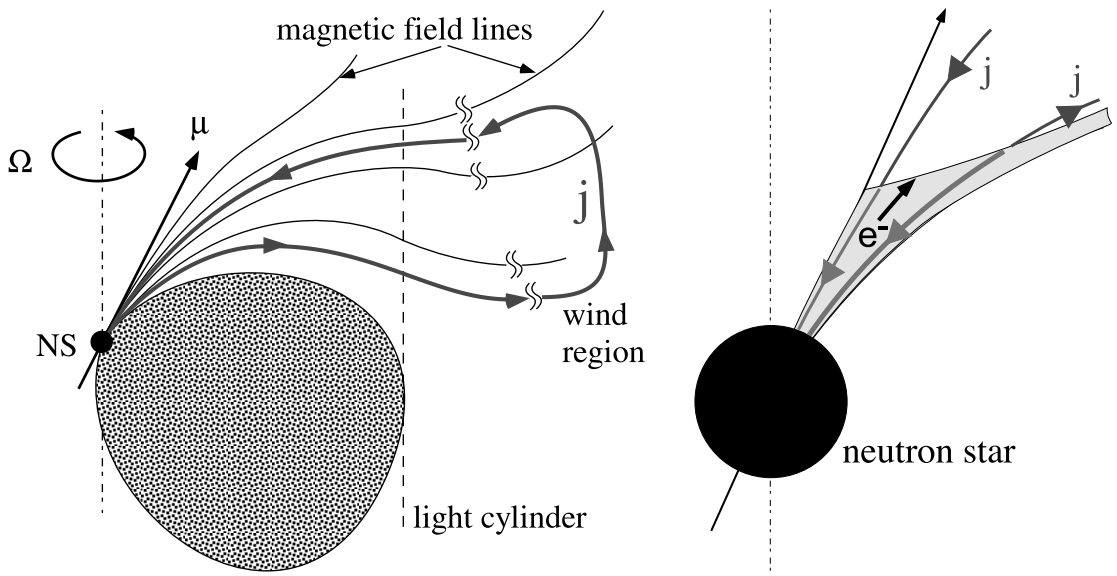


FIG. 2.—Schematic picture of electric current in the pulsar magnetosphere. *Left*: Global electric current due to the EMF exerted on the spinning neutron star surface when $\mathbf{\Omega} \cdot \boldsymbol{\mu} > 0$. *Right*: Current (*downward arrows*) derived in the inner-slot gap (*shaded region*). [*See the electronic edition of the Journal for a color version of this figure.*]

2.1. *Background Geometry*

Around a rotating neutron star with angular frequency Ω, mass M, and moment of inertia I, the background spacetime geometry is given by (Lense & Thirring 1918)

$$ds^2 = g_{tt}\,dt^2 + 2g_{t\varphi}\,dt\,d\varphi + g_{rr}\,dr^2 + g_{\theta\theta}\,d\theta^2 + g_{\varphi\varphi}\,d\varphi^2, \quad (1)$$

where

$$g_{tt} \equiv \left(1 - \frac{r_g}{r}\right)c^2, \qquad g_{t\varphi} \equiv ac\frac{r_g}{r}\sin^2\theta, \quad (2)$$

$$g_{rr} \equiv -\left(1 - \frac{r_g}{r}\right)^{-1}, \quad g_{\theta\theta} \equiv -r^2, \quad g_{\varphi\varphi} \equiv -r^2\sin^2\theta; \quad (3)$$

$r_g \equiv 2GM/c^2$ indicates the Schwarzschild radius, and $a \equiv I\Omega/(Mc)$ parameterizes the stellar angular momentum; second and higher order terms in the expansion of a/r_g are neglected. At radial coordinate r, the inertial frame is dragged at angular frequency

$$\omega \equiv -\frac{g_{t\varphi}}{g_{\varphi\varphi}} = \frac{I}{Mr_*^2}\frac{r_g}{r_*}\left(\frac{r_*}{r}\right)^3\Omega = 0.15\Omega I_{45}r_6^{-3}, \quad (4)$$

where r_* represents the stellar radius, $I_{45} \equiv I/10^{45}$ ergs cm^2, and $r_6 \equiv r/10$ km.

2.2. *Poisson Equation for Electrostatic Potential*

The first kind of equation we have to consider is the Poisson equation for the electrostatic potential, which is given by Gauss's law as

$$\nabla_\mu F^{t\mu} = \frac{1}{\sqrt{-g}}\partial_\mu\left[\frac{\sqrt{-g}}{\rho_w^2}g^{\mu\nu}\left(-g_{\varphi\varphi}F_{t\nu} + g_{t\varphi}F_{\varphi\nu}\right)\right] = \frac{4\pi}{c^2}\rho, \quad (5)$$

where ∇ denotes the covariant derivative, the Greek indices run over t, r, θ, and φ, $(-g)^{1/2} = \left(g_{rr}g_{\theta\theta}\rho_w^2\right)^{1/2} = cr^2\sin\theta$, and

$$\rho_w^2 \equiv g_{t\varphi}^2 - g_{tt}g_{\varphi\varphi} = c^2\left(1 - \frac{r_g}{r}\right)r^2\sin^2\theta. \quad (6)$$

If there is an ion emission from the stellar surface into the magnetosphere, the total real charge density ρ is given by

$$\rho = \rho_e + \rho_{\rm ion}, \quad (7)$$

where ρ_e denotes the sum of positronic and electronic charge densities, while $\rho_{\rm ion}$ does the ionic one. The six independent components of the field-strength tensor give the electromagnetic field observed by a distant static observer (not by the zero-angular-momentum observer) such that (Camenzind 1986a, 1986b)

$$E_r = F_{rt}, \quad E_\theta = F_{\theta t}, \quad E_\varphi = F_{\varphi t}, \quad (8)$$

$$B^r = \frac{g_{tt} + g_{t\varphi}\Omega}{\sqrt{-g}}F_{\theta\varphi}, \; B^\theta = \frac{g_{tt} + g_{t\varphi}\Omega}{\sqrt{-g}}F_{\varphi r}, \; B_\varphi = -\frac{\rho_w^2}{\sqrt{-g}}F_{r\theta}, \quad (9)$$

where $F_{\mu\nu} \equiv A_{\nu,\mu} - A_{\mu,\nu}$ and $A_{\mu,\nu}$ denotes the vector potential A_μ partially differentiated with respect to x^ν. The strength of the poloidal component of the magnetic field is defined as

$$B_p \equiv c^2\frac{\sqrt{-g_{rr}(B^r)^2 - g_{\theta\theta}(B^\theta)^2}}{g_{tt} + g_{t\varphi}\Omega}. \quad (10)$$

Assuming that the electromagnetic fields are unchanged in the corotating frame, we can introduce the noncorotational potential Ψ such that

$$F_{\mu t} + \Omega F_{\mu\varphi} = -\partial_\mu\Psi(r, \theta, \varphi - \Omega t), \quad (11)$$

where $\mu = t, r, \theta, \varphi$. If $F_{At} + \Omega F_{A\varphi} = 0$ holds for $A = r, \theta$, the angular frequency Ω of a magnetic field is conserved along the field line. On the neutron-star surface, we impose $F_{\theta t} + \Omega F_{\theta\varphi} = 0$ (perfect conductor) to find that the surface is equipotential; that is, $\partial_\theta\Psi = \partial_t\Psi + \Omega\partial_\varphi\Psi = 0$ holds. However, in a particle acceleration region, $F_{At} + \Omega F_{A\varphi}$ deviates from 0 and the magnetic field does not rigidly rotate (even though the deviation from uniform rotation is small when the potential drop in the gap is much less than the EMF exerted on the spinning neutron star surface). The deviation is expressed in terms of Ψ, which gives the strength of the acceleration electric field that is measured by a distant static observer as

$$E_\parallel \equiv \frac{\boldsymbol{B}}{B}\cdot\boldsymbol{E} = \frac{B^i}{B}(F_{it} + \Omega F_{i\varphi}) = \frac{\boldsymbol{B}}{B}\cdot(-\nabla\Psi), \quad (12)$$

where the Latin index i runs over spatial coordinates r, θ, φ, and an identity $B^rF_{r\varphi} + B^\theta F_{\theta\varphi} = 0$ is used.

Substituting equation (11) into equation (5), we obtain the Poisson equation for the noncorotational potential,

$$-\frac{c^2}{\sqrt{-g}}\partial_\mu\left(\frac{\sqrt{-g}}{\rho_w^2}g^{\mu\nu}g_{\varphi\varphi}\partial_\nu\Psi\right) = 4\pi(\rho - \rho_{\rm GJ}), \quad (13)$$

where the general relativistic GJ charge density is defined as

$$\rho_{\rm GJ} \equiv \frac{c^2}{4\pi\sqrt{-g}}\partial_\mu\left[\frac{\sqrt{-g}}{\rho_w^2}g^{\mu\nu}g_{\varphi\varphi}(\Omega - \omega)F_{\varphi\nu}\right]. \quad (14)$$

Using $g^{rr} = 1/g_{rr}$, $g^{\theta\theta} = 1/g_{\theta\theta}$, $g^{r\theta} = g^{\theta r} = 0$, $g^{tt} = -g_{\varphi\varphi}/\rho_w^2$, $g^{\varphi t} = g_{t\varphi}/\rho_w^2$, and $g^{\varphi\varphi} = -g_{tt}/\rho_w^2$, taking the limit $r \gg r_g$, and noting that $\partial_r[r(-g_{\theta\theta})^{1/2}B^\theta] - \partial_\theta[(-g_{rr})^{1/2}B^r]$ gives the toroidal component of $\nabla \times \boldsymbol{B}$, we find that equation (14) reduces to the ordinary, special relativistic expression of the GJ charge density (Goldreich & Julian 1969; Mestel 1971).

Instead of (r, θ, φ), we adopt in this paper the magnetic coordinates (s, θ_*, φ_*) such that s denotes the distance along a magnetic field line, and θ_* and φ_* represent the magnetic colatitude and the magnetic azimuth of the point where the field line intersects the stellar surface, respectively. Defining that $\theta_* = 0$ corresponds to the magnetic axis and $\varphi_* = 0$ to the plane on which both the rotation and the magnetic axes reside, we can compute spherical coordinate variables as

$$r(s, \theta_*, \varphi_*) = r_* + \int_0^s \frac{B^r(s', \theta, \varphi - \Omega t)}{B(s', \theta, \varphi - \Omega t)}\,ds', \quad (15)$$

$$\theta(s, \theta_*, \varphi_*) = \theta(0, \theta_*, \varphi_*) + \int_0^s \frac{B^\theta(s', \theta, \varphi - \Omega t)}{B(s', \theta, \varphi - \Omega t)}\,ds', \quad (16)$$

$$\varphi(s, \theta_*, \varphi_*) - \Omega t = \varphi_* + \int_0^s \frac{B^\varphi(s', \theta, \varphi - \Omega t)}{B(s', \theta, \varphi - \Omega t)}\,ds', \quad (17)$$

where $\theta(0, \theta_*, \varphi_*)$ satisfies $\sin\theta(0, \theta_*, \varphi_*)\cos\varphi_*\sin\alpha_{\rm inc} + \cos\theta(0, \theta_*, \varphi_*)\cos\alpha_{\rm inc} = \cos\theta_*$; $\alpha_{\rm inc}$ represents the angle between the rotation and magnetic axes. We can numerically compute the transformation matrix $\partial x^i/\partial x^{j'}$ and its inverse $\partial x^{i'}/\partial x^j$

from equations (15)–(17), where $x^1 = r, x^2 = \theta, x^3 = \varphi, x^{1'} = s$, $x^{2'} = \theta_*$, and $x^{3'} = \varphi_*$. Substituting

$$\frac{\partial}{\partial x^i} = \frac{\partial s}{\partial x^i}\frac{\partial}{\partial s} + \frac{\partial \theta_*}{\partial x^i}\frac{\partial}{\partial \theta_*} + \frac{\partial \varphi_*}{\partial x^i}\frac{\partial}{\partial \varphi_*} \tag{18}$$

into equation (13), and utilizing $\partial/\partial t = -\Omega\partial/\partial\varphi$, we obtain the following form of Poisson equation, which can be applied to arbitrary magnetic field configurations:

$$-\frac{c^2 g_{\varphi\varphi}}{\rho_w^2}(g^{ss}\partial_s^2 + g^{\theta_*\theta_*}\partial_{\theta_*}^2 + g^{\varphi_*\varphi_*}\partial_{\varphi_*}^2 + 2g^{s\theta_*}\partial_s\partial_{\theta_*} + 2g^{\theta_*\varphi_*}\partial_{\theta_*}\partial_{\varphi_*} + 2g^{\varphi_* s}\partial_{\varphi_*}\partial_s)\Psi - \left(A^s\partial_s + A^{\theta_*}\partial_{\theta_*} + A^{\varphi_*}\partial_{\varphi_*}\right)\Psi = 4\pi(\rho - \rho_{\rm GJ}), \tag{19}$$

where (see Appendix for explicit expressions)

$$g^{i'j'} = g^{\mu\nu}\frac{\partial x^{i'}}{\partial x^\mu}\frac{\partial x^{j'}}{\partial x^\nu} = g^{rr}\left(\frac{\partial x^{i'}}{\partial r}\right)_{\theta,\varphi}\left(\frac{\partial x^{j'}}{\partial r}\right)_{\theta,\varphi} + g^{\theta\theta}\left(\frac{\partial x^{i'}}{\partial \theta}\right)_{\varphi,r}\left(\frac{\partial x^{j'}}{\partial \theta}\right)_{\varphi,r} - \frac{k_0}{\rho_w^2}\left(\frac{\partial x^{i'}}{\partial \varphi}\right)_{r,\theta}\left(\frac{\partial x^{j'}}{\partial \varphi}\right)_{r,\theta} \tag{20}$$

and

$$A^{i'} \equiv \frac{c^2}{\sqrt{-g}}\left\{\partial_r\left[\frac{g_{\varphi\varphi}}{\rho_w^2}\sqrt{-g}g^{rr}\left(\frac{\partial x^{i'}}{\partial r}\right)_{\theta,\varphi}\right] + \partial_\theta\left[\frac{g_{\varphi\varphi}}{\rho_w^2}\sqrt{-g}g^{\theta\theta}\left(\frac{\partial x^{i'}}{\partial \theta}\right)_{\varphi,r}\right]\right\} - \frac{c^2 g_{\varphi\varphi}}{\rho_w^2}\frac{k_0}{\rho_w^2}\left(\frac{\partial^2 x^{i'}}{\partial \varphi^2}\right)_{r,\theta}. \tag{21}$$

The light surface, which is a generalization of the light cylinder, is obtained by setting $k_0 \equiv g_{tt} + 2g_{t\varphi}\Omega + g_{\varphi\varphi}\Omega^2$ to be zero (e.g., Znajek 1977; Takahashi et al. 1990). It follows from equation (12) that the acceleration electric field is given by $E_\parallel = -(\partial\Psi/\partial s)_{\theta_*,\varphi_*}$.

Let us briefly consider equation (19) near the polar cap surface of a nearly aligned rotator. Since $s \approx r - r_*$, $\theta \ll 1$, and $B_\varphi B^\varphi \ll B^2$, we obtain (Scharlemann et al. 1978, hereafter SAF78; Muslimov & Tsygan 1992, hereafter MT92)

$$-\frac{1}{r^2}\frac{\partial}{\partial r}\left(r^2\frac{\partial\Psi}{\partial r}\right) - \frac{1}{r^2(1 - r_g/r)}\left(\frac{\partial\theta_*}{\partial\theta}\right)^2_{\varphi,r} \times\left[\frac{1}{\theta_*}\frac{\partial}{\partial\theta_*}\left(\theta_*\frac{\partial\Psi}{\partial\theta_*}\right) + \frac{1}{\theta_*^2}\frac{\partial^2\Psi}{\partial\varphi_*^2}\right] = 4\pi(\rho - \rho_{\rm GJ}). \tag{22}$$

Noting that the solid angle element in the metric of magnetic coordinates is given by (to the lowest order in θ^2)

$$g_{\theta_*\theta_*}\,d\theta_*^2 + g_{\varphi_*\varphi_*}\,d\varphi_*^2 = r_*^2\frac{B(0,\,\theta_*,\,\varphi_*)}{B(s,\,\theta_*,\,\varphi_*)}\left(d\theta_*^2 + \sin^2\theta_* d\varphi_*^2\right), \tag{23}$$

we find that the factor

$$g^{\theta_*\theta_*} = \frac{1}{r^2}\left(\frac{\partial\theta_*}{\partial\theta}\right)^2_{\varphi,r} = \frac{1}{r_*^2}\frac{B(s,\,\theta_*,\,\varphi_*)}{B(0,\,\theta_*,\,\varphi_*)} \tag{24}$$

expresses the effect of magnetic field expansion in equation (22). In the same manner, in the general equation (19), magnetic field expansion effect is essentially contained in $g^{\theta_*\theta_*}$, $g^{\theta_*\varphi_*}$, and $g^{\varphi_*\varphi_*}$, or equivalently, in the coefficients of the second-order transfield derivatives. In what follows, we assume that the azimuthal dimension is large compared with the meridional dimension and neglect φ_* dependences.

2.3. *Particle Boltzmann Equations*

The second kind of equations we have to consider is the Boltzmann equations for particles. At time t, position $\boldsymbol{r}$, and momentum $\boldsymbol{p}$, the distribution function N_+ of positrons (or N_- of electrons) obeys the following Boltzmann equation:

$$\frac{\partial N_\pm}{\partial t} + \boldsymbol{v}\cdot\nabla N_\pm + \left(q\boldsymbol{E} + \frac{\boldsymbol{v}}{c}\times\boldsymbol{B}\right)\cdot\frac{\partial N_\pm}{\partial\boldsymbol{p}} = S_\pm(t,\,\boldsymbol{r},\,\boldsymbol{p}), \tag{25}$$

where $\boldsymbol{v} \equiv \boldsymbol{p}/(m_e\Gamma)$; m_e refers to the rest mass of the electron, q the charge on the particle, and $\Gamma \equiv 1/\left[1 - (|\boldsymbol{v}|/c)^2\right]^{1/2}$ is the Lorentz factor. In a pulsar magnetosphere, the collision term S_+ (or S_-) consists of the terms representing the appearing and disappearing rates of positrons (or electrons) at $\boldsymbol{r}$ and $\boldsymbol{p}$ per unit time per unit phase-space volume due to pair creation, pair annihilation, and the energy transfer due to IC scatterings and synchrocurvature process.

Imposing a stationary condition

$$\frac{\partial}{\partial t} + \Omega\frac{\partial}{\partial\phi} = 0, \tag{26}$$

utilizing $\nabla\cdot\boldsymbol{B} = 0$, and introducing dimensionless particle densities per unit magnetic flux tube such that $n_\pm = N_\pm/(\Omega B/2\pi ce)$, we can reduce the particle Boltzmann equations as

$$c\cos\chi\frac{\partial n_\pm}{\partial s} + \frac{dp}{dt}\frac{\partial n_\pm}{\partial p} + \frac{d\chi}{dt}\frac{\partial n_\pm}{\partial\chi} = S_\pm, \tag{27}$$

where the upper and lower signs correspond to the positrons (with charge $q = +e$) and electrons ($q = -e$), respectively; $p \equiv |\boldsymbol{p}|$ and

$$\frac{dp}{dt} \equiv qE_\parallel\cos\chi - \frac{P_{\rm SC}}{c}, \tag{28}$$

$$\frac{d\chi}{dt} \equiv -\frac{qE_\parallel\sin\chi}{p} + c\frac{\partial\left(\ln B^{1/2}\right)}{\partial s}\sin\chi, \tag{29}$$

$$\frac{ds}{dt} = c\cos\chi. \tag{30}$$

(Introduction of the radiation-reaction force, $P_{\rm SC}/c$, is discussed in the next paragraph.) For outward- (or inward-) migrating particles, $\cos\chi > 0$ (or $\cos\chi < 0$). Since we consider relativistic particles, we obtain $\Gamma = p/(m_e c)$. The second term on the right-hand side of equation (29) shows that the particle's pitch angle evolves due to the variation of B (e.g., § 12.6 of Jackson 1962, p. 591). For example, without $E_\parallel$, inward-migrating particles would be reflected by the magnetic mirrors. Using $n_\pm$, we can express ρ_e as

$$\rho_e = \frac{\Omega B}{2\pi c}\iint[n_+(s,\theta_*,\varphi_*,\Gamma,\chi) - n_-(s,\,\theta_*,\,\varphi_*,\,\Gamma,\,\chi)]\,d\Gamma\,d\chi. \tag{31}$$

The radiation-reaction force due to synchrocurvature radiation is given by (Cheng & Zhang 1996; Zhang & Cheng 1997)

$$\frac{P_{\rm SC}}{c} = \frac{e^2\Gamma^4 Q_2}{12 r_c}\left(1+\frac{7}{r_c^2 Q_2^2}\right), \tag{32}$$

where

$$r_c \equiv \frac{c^2}{(r_B+\rho_c)(c\cos\chi/\rho_c)^2 + r_B\omega_B^2}, \tag{33}$$

$$Q_2^2 \equiv \frac{1}{r_B}\left(\frac{r_B^2+\rho_c r_B - 3\rho_c^2}{\rho_c^3}\cos^4\chi + \frac{3}{\rho_c}\cos^2\chi + \frac{1}{r_B}\sin^4\chi\right), \tag{34}$$

$$r_B \equiv \frac{\Gamma m_e c^2 \sin\chi}{eB}, \qquad \omega_B \equiv \frac{eB}{\Gamma m_e c}, \tag{35}$$

and ρ_c is the curvature radius of the magnetic field line. In the limit of $\chi \to 0$ (or $\rho_c \to \infty$), equation (32) becomes the expression of pure curvature (or pure synchrotron) emission.

Let us briefly discuss the inclusion of the radiation-reaction force, $P_{\rm SC}/c$, in equation (28). Except for the vicinity of the star, the magnetic field is much less than the critical value ($B_{\rm cr} \equiv 4.41 \times 10^{13}$ G) so that quantum effects can be neglected in synchrotron radiation. Thus, we regard the radiation-reaction force, which is continuous, as an external force acting on a particle. Near the star, if $\Gamma(B/B_{\rm cr})\sin\chi > 0.1$ holds, the energy loss rate decreases from the classical formula (Erber 1966). If $\Gamma(B/B_{\rm cr})\sin\chi > 1$ holds very close to the star, the particle motion perpendicular to the field is quantized and the emission is described by the transitions between Landau states; thus, equations (28) and (32) break down. In this case, we artificially put $\chi = 10^{-20}$, which guarantees pure curvature radiation after the particles have fallen onto the ground-state Landau level, avoiding discussions of the detailed quantum effects in the strong-B region. This treatment will not affect the main conclusions of this paper, because the gap electrodynamics is governed by the pair creation taking place not very close to the star.

Collision terms are expressed as

$$\begin{aligned} S_\pm(s,\theta_*,\varphi_*,\Gamma,\chi) = & -\int_{-1}^{1} d\mu_c \int_{E_\gamma<\Gamma} dE_\gamma \eta_{\rm IC}^{\gamma}(E_\gamma,\Gamma,\mu_c) n_\pm(s,\theta_*,\varphi_*,\Gamma,\chi) \\ & + \int_{-1}^{1} d\mu_c \int_{\Gamma_i>\Gamma} d\Gamma_i\, \eta_{\rm IC}^{e}(\Gamma_i,\Gamma,\mu_c) n_\pm(s,\theta_*,\varphi_*,\Gamma_i,\chi) \\ & + \int_{-1}^{1} d\mu_c \int dE_\gamma \\ & \times \left\{\left[\frac{\partial\eta_{\gamma\gamma}(E_\gamma,\Gamma,\mu_c)}{\partial\Gamma} + \frac{\partial\eta_{\gamma B}(E_\gamma,\Gamma,\mu_c)}{\partial\Gamma}\right]\frac{B_*}{B} g_\pm(\boldsymbol{r},\ E_\gamma,\boldsymbol{k})\right\}, \end{aligned} \tag{36}$$

where μ_c refers to the cosine of the collision angle between the particles and the soft photons for inverse Compton scatterings (ICS), between the γ-rays and the soft photons for two-photon pair creation, and between the γ-rays and the local magnetic field lines for one-photon pair creation. The function g represents the γ-ray distribution function divided by $\Omega B_*/(2\pi ce)$ at energy E_γ, momentum $\boldsymbol{k}$, and position $\boldsymbol{r}$, where B_* denotes the polar-cap magnetic field strength. Here $\boldsymbol{k}$ should be understood to represent the photon propagation direction, because E_γ and $\boldsymbol{k}$ are related with the dispersion relation (see § 2.4). Since pair annihilation is negligible, we do not include this effect in equation (36).

If we multiply $d\Gamma$ on both sides of equation (36), the first (or the second) term on the right-hand side represents the rate of particles disappearing from (or appearing into) the energy interval $m_e c^2\Gamma$ and $m_e c^2(\Gamma + d\Gamma)$ due to IC scatterings; the third term does the rate of two-photon and one-photon pair creation processes.

The IC redistribution function $\eta_{\rm IC}^{\gamma}(E_\gamma,\Gamma,\mu_c)$ represents the probability that a particle with Lorentz factor Γ upscatters photons into energies between E_γ and $E_\gamma + dE_\gamma$ per unit time when the collision angle is $\cos^{-1}\mu_c$. On the other hand, $\eta_{\rm IC}^{e}(\Gamma_i,\Gamma,\mu_c)$ describes the probability that a particle changes Lorentz factor from Γ_i to Γ in a scattering. Thus, energy conservation gives

$$\eta_{\rm IC}^{e}(\Gamma_i,\Gamma_f,\mu_c) = \eta_{\rm IC}^{\gamma}\left[(\Gamma_i-\Gamma_f)m_e c^2,\Gamma_i,\mu_c\right]. \tag{37}$$

The quantity $\eta_{\rm IC}^{\gamma}$ is defined by the soft photon flux dF_s/dE_s and the Klein-Nishina cross section $\sigma_{\rm KN}$ as follows (HHS03):

$$\begin{aligned} \eta_{\rm IC}^{\gamma}(E_\gamma,\Gamma,\mu_c) = & (1-\beta\mu_c) \\ & \times \int_{E_{\rm min}}^{E_{\rm max}} dE_s \frac{dF_s}{dE_s}\int_{b_{i-1}}^{b_i} dE_\gamma \frac{dE'_\gamma}{dE_\gamma}\int_{-1}^{1} d\Omega'_\gamma \frac{d\sigma'_{\rm KN}\left(E_\gamma,\Gamma,\mu_c\right)}{dE'_\gamma\, d\Omega'_\gamma}, \end{aligned} \tag{38}$$

where $\beta \equiv (1-1/\Gamma^2)^{1/2}$ is virtually unity, Ω_γ is the solid angle of upscattered photon, the prime denotes the quantities in the electron (or positron) rest frame, and $E_\gamma = (b_{i-1}+b_i)/2$. In the rest frame of a particle, a scattering always takes place well above the resonance energy. Thus, the Klein-Nishina cross section can be applied to the present problem. The soft photon flux per unit photon energy E_s (in units of $\rm s^{-1}\ cm^{-2}$) is written as dF_s/dE_s and is given by the surface blackbody emission with redshift corrections at each distance from the star.

The differential pair-creation redistribution function is given by

$$\frac{\partial\eta_{\gamma\gamma}}{\partial\Gamma}(E_\gamma,\Gamma,\mu_c) = (1-\mu_c)\int_{E_{\rm th}}^{\infty} dE_s \frac{dF_s}{dE_s}\frac{d\sigma_p(E_\gamma,\Gamma,\mu_c)}{d\Gamma}, \tag{39}$$

where the pair-creation threshold energy is defined by

$$E_{\rm th} \equiv \frac{2}{1-\mu_c}\frac{1}{E_\gamma}, \tag{40}$$

and the differential cross section is given by

$$\begin{aligned} \frac{d\sigma_p}{d\Gamma} = & \frac{3}{8}\sigma_{\rm T}\frac{1-\beta_{\rm CM}^2}{E_\gamma} \\ & \times \left[\frac{1+\beta_{\rm CM}^2(2-\mu_{\rm CM}^2)}{1-\beta_{\rm CM}^2\mu_{\rm CM}^2} - \frac{2\beta_{\rm CM}^4(1-\mu_{\rm CM}^2)^2}{(1-\beta_{\rm CM}^2\mu_{\rm CM}^2)^2}\right]; \end{aligned} \tag{41}$$

$\sigma_{\rm T}$ refers to the Thomson cross section, and the center-of-mass quantities are defined as

$$\mu_{\rm CM} \equiv \pm\frac{2\Gamma m_e c^2 - E_\gamma}{\beta_{\rm CM}E_\gamma}, \quad \beta_{\rm CM}^2 \equiv 1 - \frac{2(m_e c^2)^2}{(1-\mu_c)E_s E_\gamma}. \tag{42}$$

Since a convenient form of $\partial\eta_{\gamma B}/\partial\Gamma$ is not given in the literature, we simply assume that all the particles are created at the

energy $\Gamma m_e c^2 = E_\gamma/2$ for magnetic pair creation. This treatment does not affect the conclusions in the present paper.

Let us briefly mention the electric current per magnetic flux tube. With projected velocities, $c\cos\chi$, along the field lines, electric current density in units of $\Omega B/(2\pi)$ is given by

$$j_{\rm gap}(s,\,\theta_*) = j_e(s,\,\theta_*) + j_{\rm ion}(\theta_*), \tag{43}$$

where

$$j_e \equiv \int\int (n_- + n_+)\cos\chi\, dp\, d\chi; \tag{44}$$

$j_{\rm ion}$ denotes the current density carried by the ions emitted from the stellar surface. Since dp/dt and $d\chi/dt$ in equation (27) depend on momentum variables p and χ, j_e and hence $j_{\rm gap}$ are not conserved along the field line in an exact sense.

Nevertheless, $j_{\rm gap}$ is kept virtually constant for s. This is because most of the particles have relativistic velocities projected along the magnetic field lines at each point. For example, consider a situation in which a pair is created inwardly at position $s = s_1$. In this case, the positron will return after migrating a certain distance (say, δs, which is positive). In $s_1 - \delta s < s < s_1$, the positron does not contribute for the electric current, because both the inward and the outward current cancel each other in a stationary situation we are dealing with, provided that the projected velocity along the field line is relativistic. Only when the positronic trajectory on (s, $p\cos\chi$) space becomes *asymmetric* with respect to the $p\cos\chi = 0$ axis, owing to the synchrotron radiation, which is important if $|\cos\chi| \ll 1$ (see Fig. 14 of Hirotani & Shibata 1999a), does the returning positron have a nonvanishing contribution for the current density at $s \sim s_1 - \delta s$. In $s > s_1$, positronic pitch angle is small enough to give a spatially constant contribution to the current density (per magnetic flux tube). For electrons, it always has an inward relativistic projected velocity and hence gives a spatially constant contribution to the current density. In practice, the contribution of the returning particles with an asymmetric trajectory around $\chi \sim 90^\circ$ on the current density, can be neglected when we discuss the $j_{\rm gap}$. Thus, we can regard $j_{\rm gap}$ as virtually conserved even though dp/dt and $d\chi/dt$ have p- and χ-dependences.

2.4. γ-Ray Boltzmann Equations

The third kind of equations we have to consider is the Boltzmann equation for γ-rays. In general, the distribution function g of the γ-rays with momentum $\boldsymbol{k}$ obeys the following Boltzmann equation:

$$\frac{\partial g}{\partial t} + c\frac{\boldsymbol{k}}{|\boldsymbol{k}|}\cdot\nabla g(t,\,\boldsymbol{r},\,\boldsymbol{k}) = S_\gamma(t,\,\boldsymbol{r},\,\boldsymbol{k}), \tag{45}$$

where $|\boldsymbol{k}|^2 \equiv -k^i k_i$; S_γ is given by

$$\begin{aligned} S_\gamma = &-\int_{-1}^{1} d\mu_c \int_1^\infty d\Gamma \frac{\partial \eta_p(\boldsymbol{r},\,\Gamma,\,\mu_c)}{\partial\Gamma} g\left(\boldsymbol{r},\,E_\gamma,\,\frac{k^\theta}{k^r},\,\frac{k^\varphi}{k^r}\right) \\ &+ \int_{-1}^{1} d\mu_c \int_1^\infty d\Gamma \eta_{\rm IC}^\gamma\left(E_\gamma,\,\Gamma,\,\mu_c\right)\frac{B}{B_*} n_\pm(s,\,\theta_*,\,\varphi_*,\,\Gamma,\,\chi) \\ &+ \int_0^\pi d\chi \int_1^\infty d\Gamma \eta_{\rm SC}\left(E_\gamma,\,\Gamma,\,\chi\right)\frac{B}{B_*} n_\pm(s,\,\theta_*,\,\varphi_*,\,\Gamma,\,\chi), \end{aligned} \tag{46}$$

where $\eta_{\rm SC}$ is the synchrocurvature radiation rate (in units of $\rm s^{-1}$) into the energy interval between E_γ and $E_\gamma + dE_\gamma$ by a particle migrating with Lorentz factor Γ, and χ is the pitch angle of the particles. An explicit expression of $\eta_{\rm SC}$ is given by Cheng & Zhang (1996).

Imposing the stationary condition (26), or equivalently, assuming that g depends on φ and t as $g = g(r,\,\theta,\,\varphi - \Omega t,\,\boldsymbol{k})$, we obtain

$$\begin{aligned} \left(c\frac{k^\varphi}{|\boldsymbol{k}|} - \Omega\right)\frac{\partial g}{\partial\bar\varphi} + c\frac{k^r}{|\boldsymbol{k}|}\frac{\partial g}{\partial r} + c\frac{k^\theta}{|\boldsymbol{k}|}\frac{\partial g}{\partial\theta} \\ = S_\gamma\left(r,\,\theta,\,\bar\varphi,\,c|\boldsymbol{k}|,\,k^r,\,k^\theta,\,k_\varphi\right), \end{aligned} \tag{47}$$

where $\bar\varphi = \varphi - \Omega t$. To compute k^i, we have to solve the photon propagation in the curved spacetime. Since the wavelength is much shorter than the typical system scales, geometrical optics gives the evolution of momentum and position of a photon by the Hamilton-Jacobi equations,

$$\frac{dk_r}{d\lambda} = -\frac{\partial k_t}{\partial r}, \quad \frac{dk_\theta}{d\lambda} = -\frac{\partial k_t}{\partial\theta}, \tag{48}$$

$$\frac{dr}{d\lambda} = \frac{\partial k_t}{\partial k_r}, \quad \frac{d\theta}{d\lambda} = \frac{\partial k_t}{\partial k_\theta}, \tag{49}$$

where the parameter λ is defined so that $c\,d\lambda$ represents the distance (i.e., line element) along the ray path. The photon energy at infinity k_t and the azimuthal wavenumber $-k_\varphi$ are conserved along the photon path in a stationary and axisymmetric spacetime (e.g., in the spacetime described by eqs. [1]–[3]). The Hamiltonian k_t can be expressed in terms of k_r, k_θ, k_φ, r, and θ from the dispersion relation $k^\mu k_\mu = 0$, which is a quadratic equation of k_μ ($\mu = t,\,r,\,\theta,\,\varphi$). Thus, we have to solve the set of four ordinary differential equations (48) and (49) for the four quantities k_r, k_θ, r, and θ along the ray. Initial conditions at the emitting point are given by $k^i/|\boldsymbol{k}| = \pm B^i/|\boldsymbol{B}|$, where $i = r,\,\theta,\,\varphi$; the upper (or lower) sign is chosen for the γ-rays emitted by an outward- (or inward-) migrating particle. When a photon is emitted with energy $E_{\rm local}$ by the particle whose angular velocity is $\dot\varphi$, it is related to k_t and $-k_\varphi$ by the redshift relation, $E_{\rm local} = (dt/d\tau)(k_t + k_\varphi\dot\varphi)$, where $dt/d\tau$ is solved from $(dt/d\tau)^2(g_{tt} + 2g_{t\varphi}\dot\varphi + g_{\varphi\varphi}\dot\varphi^2) = 1$. To express the energy dependence of g, we regard g as a function of $k_t = E_\gamma$ (i.e., observed photon energy).

In this paper, in accordance with the two-dimensional analysis of equations (19) and (27), we neglect the $\bar\varphi$-dependence of g, by ignoring the first term in the left-hand side of equation (47). In addition, we neglect the aberration of photons and simply assume that the γ-rays do not have angular momenta and put $k_\varphi = 0$. The aberration effects are important when we discuss how the outward-directed γ-rays will be observed. However, they can be correctly taken into account only when we compute the propagation of emitted photons in the three-dimensional magnetosphere. Moreover, they are not essential when we investigate the electrodynamics, because the pair creation is governed by the specific intensity of inward-directed γ-rays, which are mainly emitted in a relatively inner region of the magnetosphere. Thus, it seems reasonable to adopt $k_\varphi = 0$ when we investigate the two-dimensional gap electrodynamics.

We linearly divide the longitudinal distance into 400 grids from $s = 0$ (i.e., stellar surface) to $s = 1.4\varpi_{\rm LC}$, and the meridional coordinate into 16 field lines from $\theta_* = \theta_*^{\rm max}$ (i.e., the last-open field line) to $\theta_* = \theta_*^{\rm min}$ (i.e., gap upper boundary), and consider only the $\varphi_* = 0$ plane (i.e., the field lines threading the stellar surface on the plane formed by the rotation and magnetic axes). To solve the particle Boltzmann equations (27), we adopt the cubic

interpolated propagation (CIP) scheme with the fractional step technique to shift the profile of the distribution functions $n_\pm$ in the direction of the velocity vector in the two-dimensional momentum space (e.g., Nakamura & Yabe 1999). To solve the γ-ray Boltzmann equation (47), on the other hand, we do not have to compute the advection of g in the momentum space, because only the spatial derivative terms remain after integrating over γ-ray energy bins, which are logarithmically divided from $\beta_1 = 0.511$ MeV to $\beta_{29} = 28.7$ TeV into 29 bins. The γ-ray propagation directions, k^θ/k^r, are divided linearly into 180 bins every $\Delta\theta_\gamma = 2^\circ$. Since the specific intensity in the ith energy bin at height $\theta_* = \theta_*^k = \theta_*^{\max} - (k/16)(\theta_*^{\max} - \theta_*^{\min})$ is given by

$$g_{i,k,l}(s) = \frac{c}{\Delta\theta_\gamma \Delta\phi_\gamma} \int_{b_{i-1}}^{b_i} g\left[s,\, \theta_*^k,\, E_\gamma,\, \left(k^\theta/k^r\right)_l\right] dE_\gamma, \quad (50)$$

the observed γ-ray energy flux at distance d is calculated as

$$F_{i,l} = \frac{\Delta y \sum_k \Delta z_k g_{i,k,l}}{d^2}, \quad (51)$$

where Δy denotes the azimuthal dimension of the gap at longitudinal distance s ($= \varpi_{\rm LC}$ in this paper), Δz_k denotes the meridional thickness between two field lines with $\theta_* = \theta_{*k}$ and θ_{*k+1}, and $i = 1, 2, 3, \ldots, 28$, $k = 1, 2, 3, \ldots, 15$, and $l = 1, 2, 3, \ldots, 180$. To compute the phase-averaged spectrum, we set the azimuthal width of the γ-ray propagation direction, $\Delta\phi_\gamma$, to be π radians.

Equation (46) describes the γ-ray absorption and creation rate within the gap. However, to compute observable fluxes, we also have to consider the synchrotron emission by the secondary, tertiary, and higher-generation pairs that are created outside of the gap. If an electron or positron is created with energy $\Gamma_0 m_e c^2$ and pitch angle χ_0, it radiates the following number of γ-rays (in units of $\Omega B_*/2\pi ce$) in energies between b_{i-1} and b_i:

$$\frac{dg_i}{dn} = \frac{2\pi ce}{\Omega B_*} \int_0^\infty dt \int_{b_{i-1}}^{b_i} \frac{1}{E_\gamma} \frac{dW}{dt\, dE_\gamma}\, dE_\gamma, \quad (52)$$

where

$$\frac{dW}{dt\, dE_\gamma} = \frac{\sqrt{3} e^3 B \sin\chi_0}{h m_e c^2} F\left(\frac{E_\gamma}{E_c}\right), \quad (53)$$

$$m_e c^2 \frac{d\Gamma}{dt} = -\frac{2}{3} \frac{e^4 B^2 \sin^2\chi_0}{m_e^2 c^3} \Gamma^2, \quad (54)$$

$$F(x) \equiv x \int_x^\infty K_{5/3}(\xi)\, d\xi; \quad (55)$$

$K_{5/3}$ is the modified Bessel function of 5/3 order, and $E_c \equiv (3h/4\pi)(eB\Gamma^2 \sin\chi_i)/(m_e c)$ is the synchrotron critical energy at Lorentz factor Γ. Substituting equations (53) and (54) into equation (52), we obtain

$$\frac{dg_i}{dn} = \frac{2\pi ce}{\Omega B_*} \frac{3\sqrt{3} m_e^2 c^3}{2heB \sin\chi_0} \int_1^{\Gamma_0} \frac{d\Gamma}{\Gamma^2} \int_{b_{i-1}/E_c}^{b_i/E_c} dy \int_y^\infty K_{5/3}(\xi)\, d\xi. \quad (56)$$

Note that we assume that particle pitch angle is fixed at $\chi = \chi_0$, because ultrarelativistic particles emit radiation mostly in the instantaneous velocity direction, preventing pitch-angle evolution. Once particles lose sufficient energy, they preferentially lose perpendicular momentum; nevertheless, such less energetic particles hardly emit synchrotron photons above MeV energies. On these grounds, to incorporate the synchrotron radiation of higher generation pairs created outside of the gap, we add $\int_1^\infty (dn/d\Gamma_0)(dg_i/dn)\, d\Gamma_0$ to compute the emission of γ-rays in the energy interval $[b_{i-1}, b_i]$ in the right-hand side of equation (45), where $dn/d\Gamma_0$ denotes the particles created between position s and $s + ds$ in the Lorentz factor interval $[\Gamma_0, \Gamma_0 + d\Gamma_0]$.

2.5. *Boundary Conditions*

In order to solve the set of partial differential equations (19), (27), and (47) for Ψ, $n_\pm$, and g, we must impose appropriate boundary conditions. We assume that the gap *lower* boundary, $\theta_* = \theta_*^{\max}$, coincides with the last open field line, which is defined by the condition that $\sin\theta(-g_{rr})^{1/2} B^r + \cos\theta(-g_{\theta\theta})^{1/2} B^\theta = 0$ is satisfied at the light cylinder on the surface $\varphi_* = 0$. Moreover, we assume that the *upper* boundary coincides with a specific magnetic field line and parameterize this field line with $\theta_* = \theta_*^{\min}$. In general, $\theta_*^{\min}$ is a function of φ_*; however, we consider only $\varphi_* = 0$ in this paper. Determining the upper boundary from physical consideration is a subtle issue, which is beyond the scope of the present paper. Therefore, we treat $\theta_*^{\min}$ as a free parameter. We measure the transfield thickness of the gap with

$$h_m \equiv \frac{\theta_*^{\max} - \theta_*^{\min}}{\theta_*^{\max}}. \quad (57)$$

If $h_m = 1.0$, it means that the gap exists along all the open field lines. On the other hand, if $h_m \ll 1$, the gap becomes transversely thin and θ_* derivatives dominate in equation (19). To describe the transfield structure, we introduce the fractional height as

$$h \equiv \frac{\theta_*^{\max} - \theta_*}{\theta_*^{\max}}. \quad (58)$$

Thus, the lower and upper boundaries are given by $h = 0$ and h_m, respectively.

The *inner* boundary is assumed to be located at the neutron star surface. For the *outer* boundary, we solve the Poisson equation to a large enough distance, $s = 1.4\varpi_{\rm LC}$, which is located outside of the light cylinder. This mathematical outer boundary is introduced only for convenience in order that the $E_\parallel$ distribution inside of the light cylinder may not be influenced by the artificially chosen outer boundary position when we solve the Poisson equation. Since the structure of the outermost part of the magnetosphere is highly unknown, we artificially set $E_\parallel = 0$ if the distance from the rotation axis, ϖ, becomes greater than $0.90\varpi_{\rm LC}$. Under this artificially suppressed $E_\parallel$ distribution in $\varpi > 0.90\varpi_{\rm LC}$, we solve the Boltzmann equations for outward-migrating particles and γ-rays in the range $0 < s < 1.4\varpi_{\rm LC}$. For inward-migrating particles and γ-rays, we solve only in the range $\varpi < 0.9\varpi_{\rm LC}$. The position of the mathematical outer boundary ($1.4\varpi_{\rm LC}$ in this case) little affects the results by virtue of the artificial boundary condition, $E_\parallel = 0$ for $\varpi > 0.9\varpi_{\rm LC}$. On the other hand, the artificial outer boundary condition, $E_\parallel = 0$ for $\varpi > 0.9\varpi_{\rm LC}$, affects the calculation of outward-directed γ-rays to some degree; nevertheless, it little affects the electrodynamics in the inner part of the gap ($s < 0.5\varpi_{\rm LC}$), which is governed by the absorption of inward-directed γ-rays.

First, to solve the elliptic-type equation (19), we impose $\Psi = 0$ on the lower, upper, and inner boundaries. At the mathematical outer boundary ($s = 1.4\varpi_{\rm LC}$), we impose $\partial\Psi/\partial s = 0$. Generally speaking, the solution of $E_\parallel = -(\partial\Psi/\partial s)_{s\to 0}$ under these boundary

conditions does not vanish at the stellar surface. Let us consider how to cancel this remaining electric field.

For a super-GJ current density in the sense that $\rho_e - \rho_{\rm GJ} < 0$ holds at the stellar surface, equation (19) gives a positive electric field near the star. In this case, we assume that ions are emitted from the stellar surface so that the additional positive charge in the thin nonrelativistic region may bring $E_\parallel$ to zero (for the possibility of free ejection of ions due to a low work function, see Jones 1985; Neuhauser et al. 1986, 1987). The column density in the nonrelativistic region becomes (SAF78)

$$\Sigma_{\rm NR} = \frac{1}{2\pi}\sqrt{\frac{c\Omega B_*}{q/m} j_{\rm ion}}, \tag{59}$$

where q/m represents the charge-to-mass ratio of the ions and $j_{\rm ion}$ gives the ionic current density in units of $\Omega B_*/(2\pi)$. Equating $4\pi\Sigma_{\rm NR}$ to $-(\partial\Psi/\partial s)_{s\to 0}$ calculated from relativistic positrons, electrons, and ions, we obtain the ion injection rate $j_{\rm ion}$ that cancels $E_\parallel$ at the stellar surface.

For a sub-GJ current density in the sense that $\rho_e - \rho_{\rm GJ} > 0$ holds at the stellar surface, Ψ increases outward near the star to peak around $s = 0.02\varpi_{\rm LC}$–$0.10\varpi_{\rm LC}$, depending on $\alpha_{\rm inc}$ and $\rho_e(s=0)$, then decreases to become negative in the outer magnetosphere. That is, $-(\partial\Psi/\partial s)_{s\to 0} < 0$ holds in the inner region of the gap. In this case, we assume that electrons are emitted from the stellar surface and fill out the region where $\Psi > 0$; thus, we artificially put $\Psi = 0$ if $\Psi > 0$ appears. Even though a nonvanishing, positive $E_\parallel$ remains at the inner boundary, which is located away from the stellar surface, we neglect such details. This is because the gap with a sub-GJ current density is found to be inactive and hence less important, as is demonstrated in § 3.

Second, to solve the hyperbolic-type equations (27) and (47), we assume that neither positrons nor γ-rays are injected across the inner boundary; thus, we impose

$$n_+\left(s^{\rm in}, \theta_*, \Gamma, \chi\right) = 0, \quad g\left(s^{\rm in}, \theta_*, E_\gamma, \theta_\gamma\right) = 0 \tag{60}$$

for arbitrary θ_*, Γ, $0 < \chi < \pi/2$, E_γ, and $\cos(\theta_\gamma - \theta_B) > 0$, where θ_B designates the outward magnetic field direction. In the same manner, at the outer boundary, we impose

$$n_-\left(s^{\rm out}, \theta_*, \Gamma, \chi\right) = 0, \quad g\left(s^{\rm out}, \theta_*, E_\gamma, \theta_\gamma\right) = 0 \tag{61}$$

for arbitrary θ_*, Γ, $\pi/2 < \chi < \pi$, E_γ, and $\cos(\theta_\gamma - \theta_B) < 0$.

3. APPLICATION TO THE CRAB PULSAR

Since the formulation described in the foregoing section is generic, we specify some of the quantities in § 3.1 before turning to a closer examination in §§ 3.2–3.8.

3.1. *Assumptions on Magnetic Field and Soft Photon Field*

First, let us specify the magnetic field. Near the star, we adopt the static (unperturbed by rotation and currents) dipole solution obtained in the Schwarzschild spacetime (e.g., MT92, and references therein). That is, in equation (9), we evaluate $F_{\theta\varphi}$ and $F_{\varphi r}$ as

$$\frac{F_{\theta\varphi}}{\sqrt{-g}} = f(r)\frac{2\mu}{r^3}\cos\Theta, \tag{62}$$

$$\frac{F_{\varphi r}}{\sqrt{-g}} = -\frac{\mu}{r^2}\frac{d}{dr}\left[\frac{f(r)}{r}\right]\sin\Theta, \tag{63}$$

where Θ is the angle measured from the magnetic axis and

$$f(r) = -3\left[\frac{1}{2}\frac{r}{r_g} + \left(\frac{r}{r_g}\right)^2 + \left(\frac{r}{r_g}\right)^3 \ln\left(1 - \frac{r_g}{r}\right)\right]. \tag{64}$$

At high altitudes (but within the light cylinder), the open field lines deviate from the static dipole to be swept back in the opposite direction of the rotation and bent toward the rotational equator. There are two important mechanisms that cause the deviation: charge flow along the open field lines, and retardation of an inclined, rotating dipole. Both of them appear as the first order correction in $\varpi/\varpi_{\rm LC}$ expansion to the static dipole. To study the former correction, Muslimov & Harding (2005) employed the space-charge-limited longitudinal current solved by MT92, and they derived an analytic solution of the correction. However, if we discard the space-charge-limited flow of emitted electrons and consider copious pair creation in the gap, we have to derive a more general correction formula that is applicable for arbitrary longitudinal current distribution. To follow up this general issue further would involve us in other factors than the electrodynamics of the accelerator and would take us beyond the scope of this paper. Thus, we consider only the latter correction and adopt the inclined, vacuum magnetic field solution obtained by CRZ00 (their eqs. [B2]–[B4]).

Second, we consider how the *toroidal* current density, $J^{\hat\varphi}$, affects $\rho_{\rm GJ}$ near the light cylinder. In the outer magnetosphere, general relativistic effects are negligible; thus, equation (14) becomes

$$\rho_{\rm GJ} = -\frac{\boldsymbol{\Omega}\cdot\boldsymbol{B}}{2\pi c} + \frac{\varpi}{\varpi_{\rm LC}}\frac{J^{\hat\varphi}}{c}. \tag{65}$$

Since $J^{\hat\varphi}$ is of the order of $(\Omega B/2\pi)(\varpi/\varpi_{\rm LC})$, the second term appears as a positive correction that is proportional to $(\varpi/\varpi_{\rm LC})^2$ and will become comparable to the first term if $\varpi/\varpi_{\rm LC} \sim 1$. Thus, to incorporate this special relativistic correction, we adopt

$$\rho_{\rm GJ} = -\frac{\boldsymbol{\Omega}\cdot\boldsymbol{B}}{2\pi c}\left[1 + \kappa\left(\frac{\varpi}{\varpi_{\rm LC}}\right)^2\right], \tag{66}$$

where the constant κ is of the order of unity. For example, CHR86a adopted $\kappa = 1$. Even though a larger value of κ is preferable to reproduce a harder curvature spectrum above 5 GeV and a larger secondary synchrotron flux around 100 MeV, we adopt a conservative value $\kappa = 0.5$ in the present paper.

Third, we have to specify the differential soft photon flux, dF_s/dE_s, which appears in equations (38) and (39). As the possible soft photon fields illuminating the gap, we can consider the following three components in general:

1. Photospheric emission from the hot surface of a cooling neutron star. For simplicity, we approximate this component with a blackbody spectrum with a single temperature, kT_s. We assume that this component is uniformly emitted from the whole neutron star surface.
2. Thermal soft X-ray emission from the neutron star's polar cap heated by the bombardment of relativistic particles streaming toward the star from the magnetosphere. Since we consider a young pulsar in this paper, this component is negligible compared to the first component.
3. Nonthermal, power-law emission from charged relativistic particles created outside of the gap in the magnetosphere. The emitted radiation can be observed from the optical to the γ-ray band. Since the nonthermal emission will be beamed away from

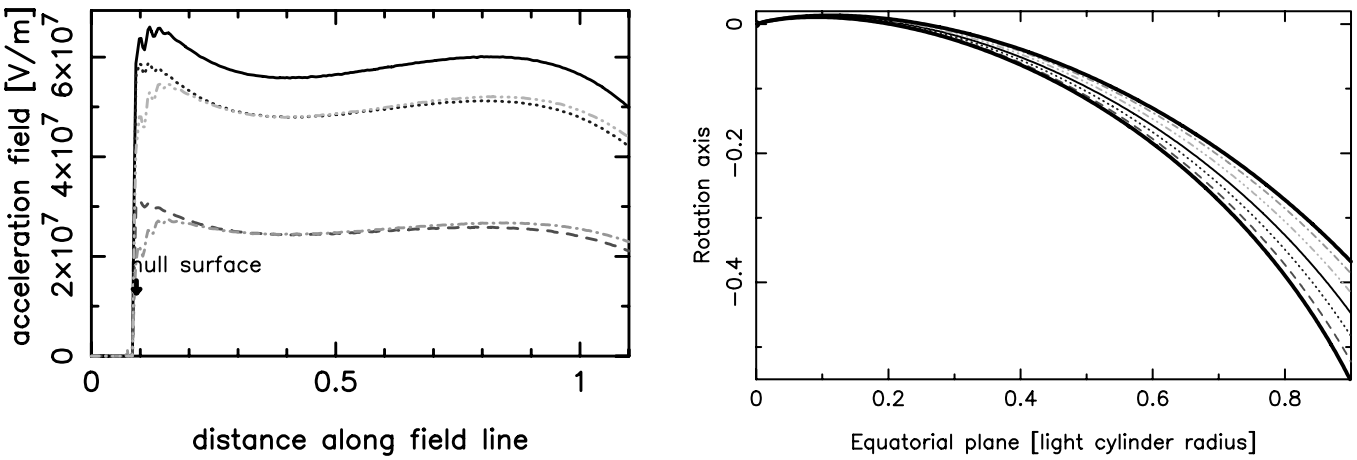


FIG. 3.—*Left*: Field-aligned electric field of a *sub*-GJ current solution at five discrete heights (see right panel) for $\alpha_{\rm inc} = 70^\circ$ and $h_m = 0.047$. The abscissa indicates the distance along the field line from the star in the unit of the light-cylinder radius. The null surface position at the height $h = h_m/2$ is indicated by the down arrow. *Right*: Magnetic field lines on the poloidal plane in which both the rotational and magnetic axes reside. Instead of $h_m = 0.047$, $h_m = 0.200$ is adopted for clarity. The thick solid curves denote the lower and upper boundaries, while the thin dashed, dotted, solid, dash–triple-dotted, and dash-dotted ones give the same h/h_m values as those in the left panel; they are $h/h_m = 2/16$, 5/16, 8/16, 11/16, and 14/16, respectively. [*See the electronic edition of the Journal for a color version of this figure.*]

the gap, we assume that this component does not illuminate the gap. The major conclusions in this paper will not be affected by this assumption, except that the pair creation would increase to suppress the potential drop and hence the γ-ray luminosity if this component illuminates the gap.

We apply the scheme to the Crab pulsar, adopting four free parameters, $\alpha_{\rm inc}$, μ, kT_s, and h_m. Other quantities such as gap geometry on the poloidal plane, exerted $E_\parallel$ and potential drop, particle density, and energy distribution, as well as the γ-ray flux and spectrum, are uniquely determined if we specify these four parameters. We consider transversely thin and thick cases in § 3.2 and §§ 3.3–3.8, respectively.

3.2. *Sub-GJ Current Solution: Traditional Outer-Gap Model*

To begin with, let us consider the magnetic inclination $\alpha_{\rm inc} = 70^\circ$, which is more or less close to the value (65°) suggested by a three-dimensional analysis in the traditional outer gap model (CRZ00). We adopt $kT_s = 100$ eV as the surface blackbody temperature, which is consistent with the observational upper limit, $kT_s < 180$ eV (Tennant et al. 2001). In §§ 3.2–3.4, we adopt $\mu = 4.0 \times 10^{30}$ G cm^3 as the magnetic dipole moment, which gives $B_* = 1.46 \times 10^{13}$ G (eq. [10]), assuming $r_* = 10^6$ cm and $M = 1.4\ M_\odot$. If we evaluate μ from the spin-down luminosity $\dot{E} = 2\Omega^4\mu^2/3c^3$, we obtain $\mu = 3.8 \times 10^{30}$ G cm^3 for $\dot{E} = 4.46 \times 10^{38}$ ergs s^{-1} (e.g., Becker & Trümper 1997). The dependence of the solution on kT_s, μ, and $\alpha_{\rm inc}$ is discussed in §§ 3.4–3.6.

Examine a sub-GJ current solution, which is defined by $j_e < |\rho_{\rm GJ}/(\Omega B/2\pi c)|_{s=0} \approx (1 - \omega/\Omega)B_{z*}/B_*$, where B_{z*} refers to the surface magnetic field component projected along the rotation axis; the right-hand side is evaluated at $s = 0$ and $\theta_* = \theta_*^{\rm max}$. To this aim, we consider a transversely thin gap, $h_m = 0.047$. The solution becomes similar to the vacuum one obtained in the traditional outer-gap model (CHR86a), as the left panel of Figure 3 indicates. In this figure, we present $E_\parallel(s, h)$ at discrete height h of $2h_m/16$, $5h_m/16$, $8h_m/16$, $11h_m/16$, and $14h_m/16$ with dashed, dotted, solid, dash–triple-dotted, and dash-dotted curves, respectively; they are depicted in the right panel with a larger h_m (= 0.200) for illustration purposes. For one thing, for such a transversely thin, nearly vacuum gap, the inner boundary is located slightly inside of the null surface. What is more, $E_\parallel$ maximizes at the central height, $h = h_m/2$, and remains roughly constant in the entire region of the gap. The solved $E_\parallel$ distributes almost symmetrically with respect to the central height; for example, the dashed and dash-dotted curves nearly overlap each other. Similar solutions are obtained for a thinner gap, $h_m < 0.047$.

3.3. *Super-GJ Current Solution: Hybrid Gap Structure*

Next, let us consider a thicker gap, $h_m = 0.048$. In this case, j_e becomes comparable to or greater than $|\rho_{\rm GJ}/(\Omega B/2\pi c)|_{s=0}$ in the upper half region $h > h_m/2$ of the gap, causing the solution to deviate from the vacuum one. In the left panel of Figure 4, we present $E_\parallel(s, h)$ at five discrete heights h in the same way as Figure 3. It follows that $E_\parallel$ is screened by the discharge of created pairs in the innermost region ($s < 0.3\varpi_{\rm LC}$) in the higher latitudes ($h > h_m/2$). For example, $E_\parallel$ at $h = 7h_m/8$ (*dash-dotted curve*) deviates from the unscreened solution at the lower latitudes $h = h_m/8$ (*dashed curve*). On the other hand, along the lower field lines ($h < h_m/2$), $E_\parallel(s)$ is roughly constant as in the traditional outer-gap model.

Let us further consider a thicker gap, $h_m = 0.060$. The right panel of Figure 4 shows that $E_\parallel(s, h)$ is substantially screened compared to the marginally super-GJ case, $h_m = 0.048$ (*left panel*). Because the gap transfield thickness virtually shrinks in $s < 0.5\varpi_{\rm LC}$ due to screening in the higher latitudes, $E_\parallel$ in the lower latitudes also decreases compared to smaller h_m cases, as the dashed lines in the left and right panels indicate.

To understand the screening mechanism, it is helpful to examine the Poisson equation (22), which is a good approximation in $s < 0.4\varpi_{\rm LC}$. In the transversely thin limit, it becomes

$$-\frac{1}{(1 - r_g/r)}\frac{1}{r_*^2}\frac{B(r)}{B_*}\frac{\partial^2\Psi}{\partial\theta_*^2} \approx 4\pi(\rho - \rho_{\rm GJ}) \approx \frac{2\Omega B(r)}{c}\left(\frac{\rho}{\Omega B/2\pi c} - \frac{\rho_{\rm GJ}}{\Omega B/2\pi c}\right). \quad (67)$$

Since we are interested in the second-order θ_* derivatives, this equation is valid not only for a nearly aligned rotator, but also for an oblique rotator. We could directly check it from the general

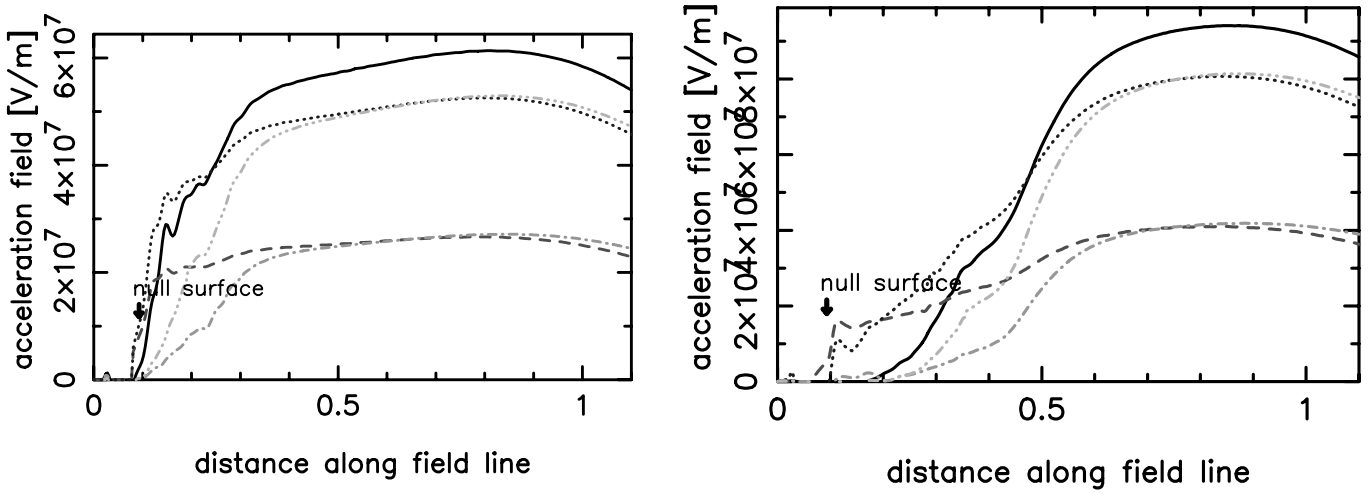


FIG. 4.—Same as Fig. 3: $E_\parallel(s, h)$ of two *super*-GJ current solutions, but for $h_m = 0.048$ (*left*) and 0.060 (*right*) at five discrete h values. [*See the electronic edition of the Journal for a color version of this figure.*]

equation (13). Factoring out the magnetic field expansion factor, $B(r)/B_*$, from the two sides, we obtain

$$\Psi \approx \left(1 - \frac{r_g}{r}\right) \frac{\Omega B_*}{c} \left(\frac{\rho}{\Omega B/2\pi c} - \frac{\rho_{\rm GJ}}{\Omega B/2\pi c}\right) \times r_*^2 \left(\theta_* - \theta_*^{\rm min}\right)\left(\theta_*^{\rm max} - \theta_*\right). \quad (68)$$

We thus find that $E_\parallel \equiv -\partial\Psi/\partial s$ is approximately proportional to $-\partial(\rho/B - \rho_{\rm GJ}/B)/\partial s$. It is, therefore, important to examine the two-dimensional distribution of ρ/B and $\rho_{\rm GJ}/B$ to understand $E_\parallel(s, h)$ behavior.

In Figure 5, we present $\rho/(\Omega B/2\pi c)$, $\rho_e/(\Omega B/2\pi c)$, and $\rho_{\rm GJ}/(\Omega B/2\pi c)$, as the solid, dash-dotted, and dashed curves, at nine discrete magnetic latitudes, ranging from $h = (4/16)h_m$, $(5/16)h_m$, . . ., to $(12/16)h_m$ for the same parameters as the right panel of Figure 4. If there is a cold-field ion emission from the star, the total charge density (*solid curve*) deviates from the created charge density (*dash-dotted curve*). It follows that the current is sub-GJ for $h \le (5/16)h_m = 0.0187$ and super-GJ for $h \ge (6/16)h_m = 0.0225$. Along the field lines with super-GJ current, $\rho_e - \rho_{\rm GJ}$ becomes negative close to the star. This inevitably leads to a positive $E_\parallel$, which extracts ions from the stellar surface. In this paper, we assume that the extracted ions consist of protons; nevertheless, the conclusions are little affected by the composition of the extracted ions.

In the outer region, ρ/B levels off in $s > 0.5\varpi_{\rm LC}$ for $h > h_m/2$. Since $\rho_{\rm GJ}/B$ becomes approximately a linear function of s, $E_\parallel$ remains nearly constant in $s > 0.5\varpi_{\rm LC}$, in the same manner as in traditional outer-gap model. In the inner region, on the other hand, inward-directed γ-rays propagate into the convex side due to the field line curvature, increasing particle density exponentially with h. As a result, the lower part (i.e., smaller h region) becomes nearly vacuum. For example, at $h = h_m/4 = 0.015$ (Fig. 5, *top left panel*), the positive $\rho_e - \rho_{\rm GJ}$ leads to a negative $E_\parallel$ at the stellar surface, inducing *no* ion emission. Even though the created current is sub-GJ at $h = 0.0187$, ions are extracted from the surface. This is because the negative $\rho_{\rm eff} \equiv \rho - \rho_{\rm GJ}$ in the higher latitudes $h \ge 0.0225$ cancels the relatively small positive $\rho_{\rm eff}$ along $h = 0.0187$ to induce a positive $E_\parallel$ at the stellar surface. Such a two-dimensional effect in the Poisson equation is also important in the higher altitudes ($0.1\varpi_{\rm LC} < s < 0.3\varpi_{\rm LC}$) along the higher-latitude field lines ($h \ge 0.0225$). Outside of the null surface, $s > 0.09\varpi_{\rm LC}$, there is a negative $\rho_{\rm eff}$ in the sub-GJ current region ($h \le 0.015$). This negative $\rho_{\rm eff}$ works to prevent $E_\parallel$ from vanishing in the higher latitudes, where pair creation is copious. However, the created pairs discharge until $E_\parallel$ vanishes, resulting in a larger gradient of ρ than that of $\rho_{\rm GJ}$ in the intermediate latitudes in $0.0225 \le h \le 0.0262$. In the upper half region ($0.03 \le h < h_m = 0.06$), $\partial\rho/\partial s$ does not have to be greater than $\partial\rho_{\rm GJ}/\partial s$ in order to screen $E_\parallel$.

In short, the gap has a hybrid structure: The lower latitudes (with small h) are nearly vacuum, having sub-GJ current densities, and the inner boundary is located slightly inside of the null surface, because the $\Psi > 0$ region will be filled with the electrons emitted from the stellar surface. The higher latitudes, on the other hand, are nonvacuum, having super-GJ current densities, and the inner boundary is located at the stellar surface, extracting ions at the rate such that their nonrelativistic column density at the stellar surface cancels the strong $E_\parallel$ induced by the negative $\rho - \rho_{\rm GJ}$ of relativistic electrons, positrons, and ions. The created pairs discharge such that $E_\parallel$ virtually vanishes in the region where pair creation is copious. Thus, in the intermediate latitudes between the sub-GJ and super-GJ regions, $\partial\rho/\partial s > \rho_{\rm GJ}/\partial s$ holds.

Even though the innermost region of the gap is inactive, general relativistic effect (spacetime dragging effect, in this case) is important to determine the ion emission rate from the stellar surface. For example, at $h = h_m/2$ for $h_m = 0.060$ (i.e., central panel in Fig. 5), $j_{\rm ion}$ is 69% greater than what would be obtained in the Newtonian limit, $\rho_{\rm GJ} = -\boldsymbol{\Omega} \cdot \boldsymbol{B}/2\pi c$. This is because the reduced $|\rho_{\rm GJ}|$ near the star (about 15% less than the Newtonian value) enhances the positive $E_\parallel$, which has to be canceled by a greater ion emission (compared to the Newtonian value). The current, $j_{\rm ion}$, is adjusted so that $|\rho_{\rm eff}|$ may balance with the transfield derivative of Ψ near the star. The resulting $|\rho_{\rm eff}|$ becomes small compared to $|\rho_{\rm GJ}|$, in the same manner as in traditional polar-cap models, which has a negative $E_\parallel$ with electron emission from the star. Although the nonrelativistic ions have a large positive charge density very close to the star (within 10 cm from the surface), it cannot be resolved in Figure 5. Note that the present calculation is performed from the stellar surface to the outer magnetosphere and does not contain a region with $E_\parallel < 0$. It follows that an accelerator having $E_\parallel < 0$ (e.g., a polar-cap or a polar-slot-gap accelerator) cannot exist along the magnetic field lines that have an super-GJ current density created by the mechanism described in the present paper.

It is worth examining how $E_\parallel$ changes with varying h_m. In Figure 6, we present $E_\parallel(s, h)$ at the central height $h = h_m/2$. In

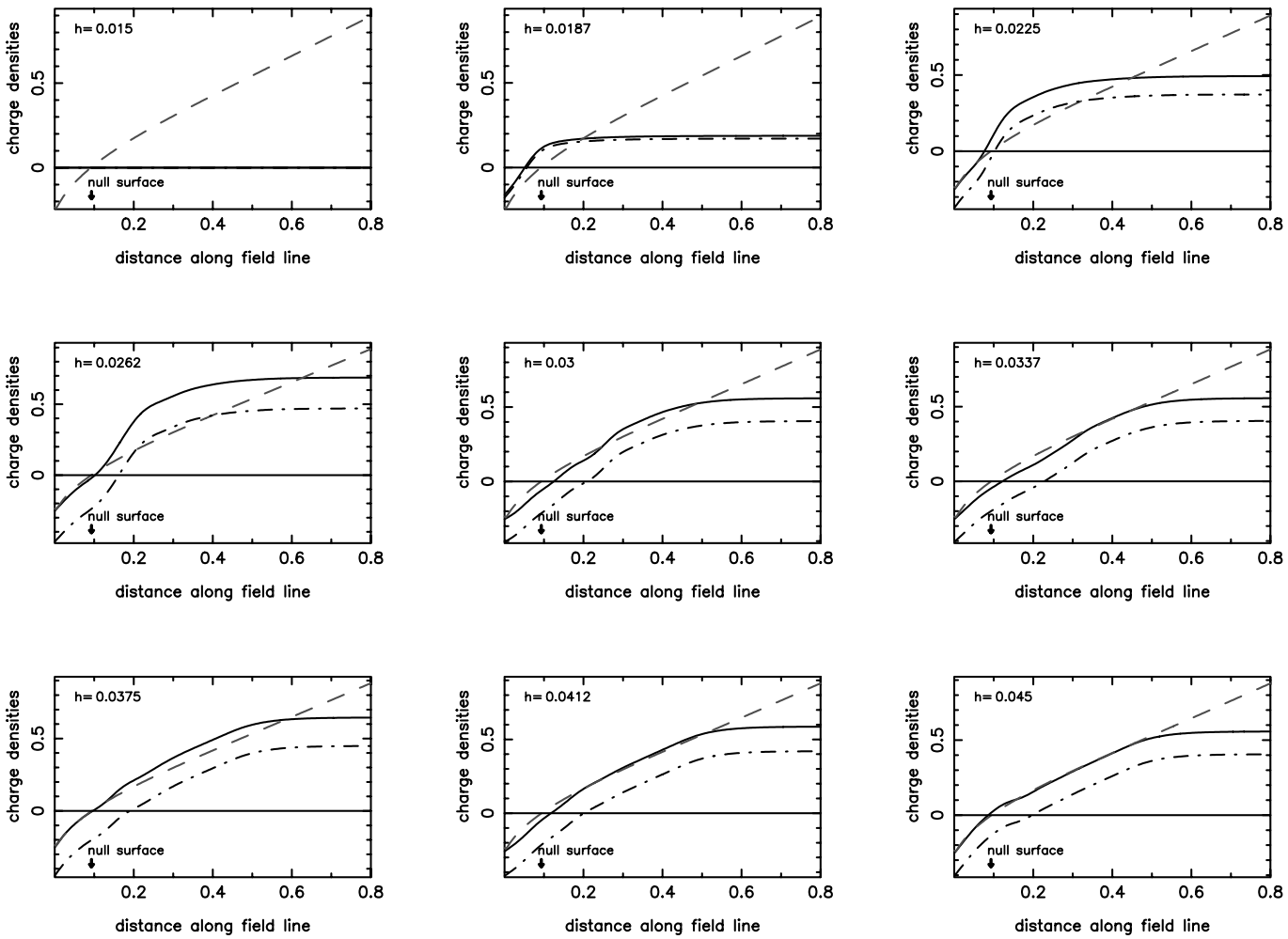


FIG. 5.—Total (*solid curves*), created (*dash-dotted curves*), and Goldreich-Julian (*dashed curves*) charge densities in $\Omega B(s,h)/(2\pi c)$ units, for $\alpha_{\rm inc} = 70^\circ$ and $h_m = 0.060$ at nine transfield heights, h. If there is an ion emission from the stellar surface, the total charge density deviates from the created one. [*See the electronic edition of the Journal for a color version of this figure*.]

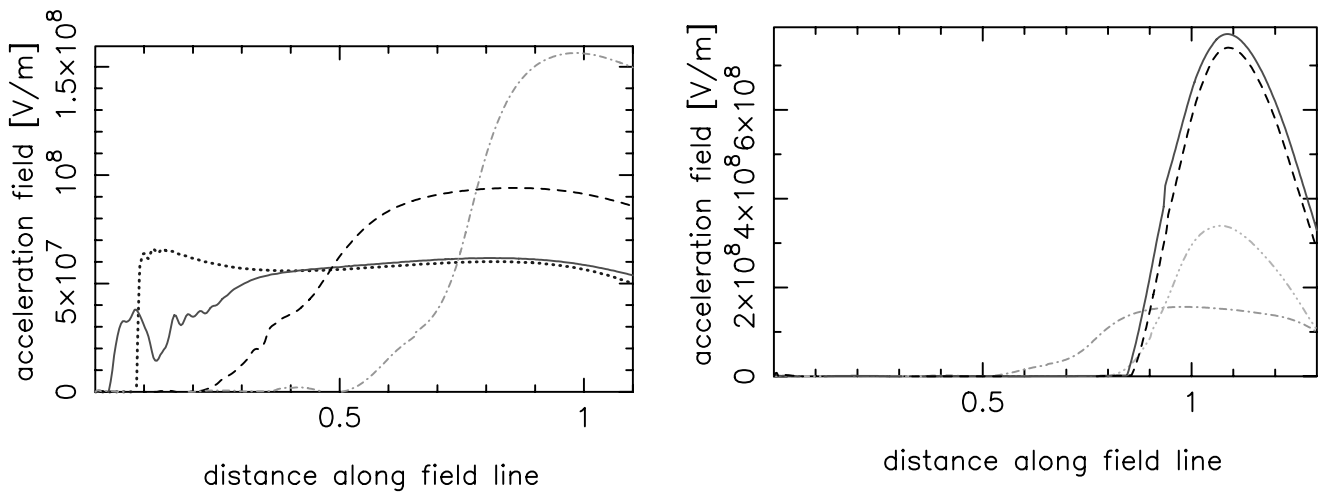


FIG. 6.—Field-aligned electric field at $h = h_m/2$ as a function of $s/\varpi_{\rm LC}$ for $\mu = 4.0 \times 10^{30}$ G cm^3, $kT_s = 100$ eV, and $\alpha_{\rm inc} = 70^\circ$. *Left*: The dotted, solid, dashed, and dash-dotted curves correspond to $h = 0.047$, 0.048, 0.060, and 0.100, respectively. *Right*: The dash-dotted, dash–triple-dotted, solid, and dashed curves correspond to $h = 0.100$, 0.160, 0.200, and 0.240, respectively. [*See the electronic edition of the Journal for a color version of this figure*.]

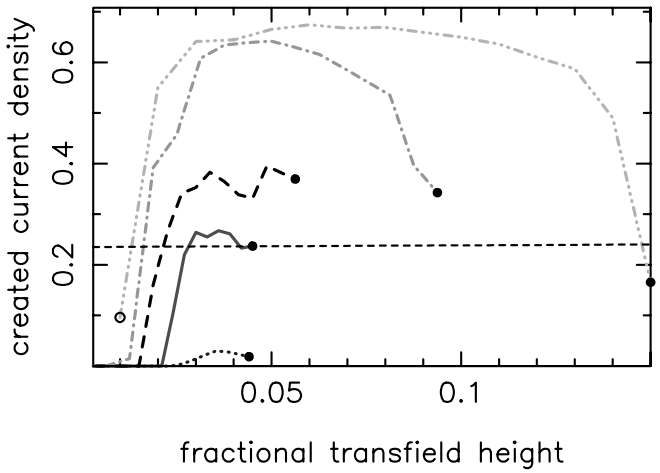


FIG. 7.—Created current density j_e (in units of $\Omega B/2\pi$) as a function of the transfield thickness h for $\mu = 4.0 \times 10^{30}$ G cm^3, $kT_s = 100$ eV, and $\alpha_{\rm inc} = 70^\circ$. The dotted, solid, dashed, dash-dotted, and dash–triple-dotted curves correspond to $h = 0.047$, 0.048, 0.060, 0.100, and 0.160, respectively. [*See the electronic edition of the Journal for a color version of this figure.*]

the left panel, the dotted, solid, dashed, and dash-dotted curves correspond to $h_m = 0.047$, 0.048, 0.060, and 0.100, respectively, while in the right panel, the dash-dotted, dash–triple-dotted, solid, and dashed curves correspond to 0.100, 0.160, 0.200, and 0.240, respectively. It follows that the inner part of the gap becomes substantially screened by the discharge of created pairs as h_m increases. It also follows that the maximum of $E_\parallel$ increases with increasing h_m for $h_m < 0.2$, because the two-dimensional screening effect due to the zero-potential walls becomes less important for a larger h_m. To solve particle and γ-ray Boltzmann equations, we artificially put $E_\parallel = 0$ in $\varpi > 0.9\varpi_{\rm LC}$, or equivalently in $s > 1.1\varpi_{\rm LC}$ for $\alpha_{\rm inc} = 70^\circ$, as mentioned in § 2.5.

The created current density, j_e, is presented in Figure 7, as a function of h. The thin dashed line represents $|\rho_{\rm GJ}/(\Omega B/2\pi c)|_{s=0}$; if j_e appears below (or above) this line, the created current is sub- (or super-) GJ along the field line specified by h. The open and filled circles denote the lowest and highest latitudes that are used in the computation. For $h_m = 0.047$, the solution (*dotted curve*) is sub-GJ along all the field lines; thus, screening due to the discharge is negligible as the dotted curve in the left panel of Figure 6 shows. As h_m increases, the solution becomes super-GJ from the higher latitudes, as indicated by the solid ($h_m = 0.048$), dashed ($h_m = 0.060$), dash-dotted ($h_m = 0.100$), and dash–triple-dotted ($h_m = 0.160$) curves in Figure 7. As a result, screening becomes significant as h_m increases, as Figure 6 shows. This screening of $E_\parallel$ has a negative feedback effect in the sense that j_e is regulated below unity. Even though it is not resolved in Figure 6, in the lower latitudes, j_e grows across the gap height exponentially, as CHR86a suggested. For example, $j_e = 3.0 \times 10^{-10}$, 2.1×10^{-9}, 2.1×10^{-8}, 1.0×10^{-7}, 4.3×10^{-7}, 1.0×10^{-6}, 4.6×10^{-5}, and 1.3×10^{-1} at $h/h_m = 1/16$, 2/16, 3/16, . . ., 8/16, respectively, for $h_m = 0.048$ (*solid curve*). This is because the pair creation rate at height h is proportional to the number of γ-rays that are emitted by charges on all field lines below h.

Let us now turn to the emitted γ-rays. Figure 8 shows the phase-averaged γ-ray spectrum calculated for three different h_m values. Open circles denote the pulsed fluxes detected by COMPTEL (below 30 MeV; Ulmer et al. 1995; Kuiper et al. 2001) and EGRET (above 30 MeV; Nolan et al. 1993; Fierro et al. 1998), while the open square does the upper limit obtained by CELESTE (de Naurois et al. 2002). It follows that the sub-GJ (i.e., traditional outer-gap) solution with $h_m = 0.047$ predicts too little γ-ray flux compared with the observations. (Note that in traditional outer-gap models, particle number density is assumed to be the GJ value, while $E_\parallel$ is given by the vacuum solution of the Poisson equation, which is inconsistent.) The maximum flux, which appears around GeV energies, does not become greater than 10^{11} Jy Hz for any sub-GJ solutions, whatever values of $\alpha_{\rm inc}$, μ, and kT_s we may choose. Thus, we can rule out the possibility of a sub-GJ solution for the Crab pulsar.

As h_m increases, the increased $E_\parallel$ results in a harder curvature spectrum, as the solutions corresponding to $h_m = 0.100$ and 0.200 indicate. As discussed in § 4.1, the problem of insufficient γ-ray fluxes may be solved if we consider a three-dimensional gap structure. However, the secondary synchrotron flux emitted outside of the gap is too small to explain the flat spectral shape below 100 MeV. The γ-ray spectrum is nearly unchanged for $0.2 \le h_m \le 0.3$. For $h_m > 0.3$, the γ-ray flux tends to decrease, because the $E_\parallel(s)$ peaks outside of the artificial outer boundary, $r \sin\theta = 0.9\varpi_{\rm LC}$, which corresponds to $s = 1.1\varpi_{\rm LC}$ for $\alpha_{\rm inc} = 70^\circ$. For $h_m > 0.4$, the gap virtually vanishes because of the discharge of copiously created pairs; in other words, the gap is located outside of $r \sin\theta = 0.9\varpi_{\rm LC}$. On these grounds, we cannot reproduce the observed flat spectral shape if we consider $kT_s = 100$ eV, $\mu = 4.0 \times 10^{30}$ G cm^3, and $\alpha_{\rm inc} = 70^\circ$, no matter what value of h_m is adopted. Therefore, in the next three subsections, we examine

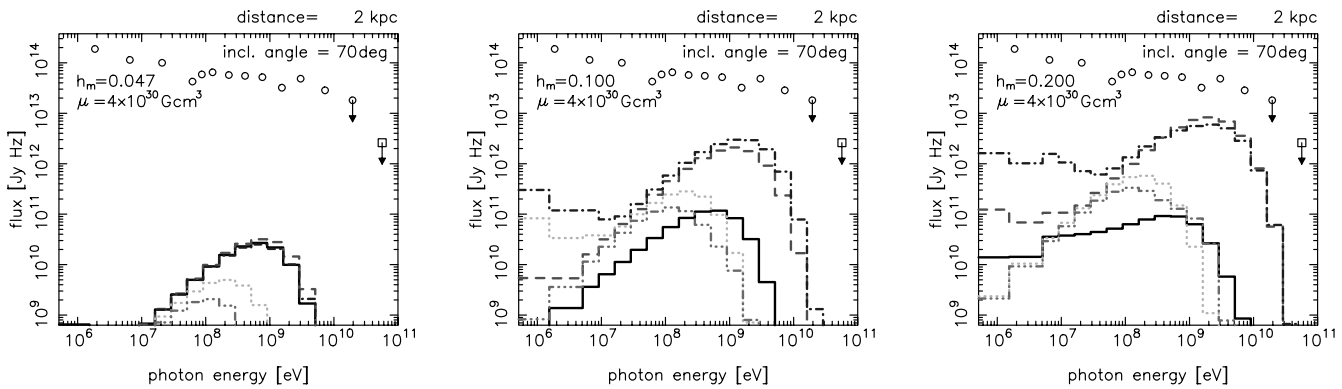


FIG. 8.—Calculated phase-averaged spectra of the pulsed, outward-directed γ-rays for $\alpha_{\rm inc} = 70^\circ$, $kT_s = 100$ eV, and $\mu = 4.0 \times 10^{30}$ G cm^3, with three different gap thickness, h_m. The flux is averaged over the meridional emission angles between 44° and 58° (*solid curve*), 58° and 72° (*dashed curve*), 72° and 86° (*dash-dotted curve*), 86° and 100° (*dotted curve*), and 100° and 114° (*dash–triple-dotted curve*), from the magnetic axis on the plane in which both the rotational and magnetic axes reside. [*See the electronic edition of the Journal for a color version of this figure.*]

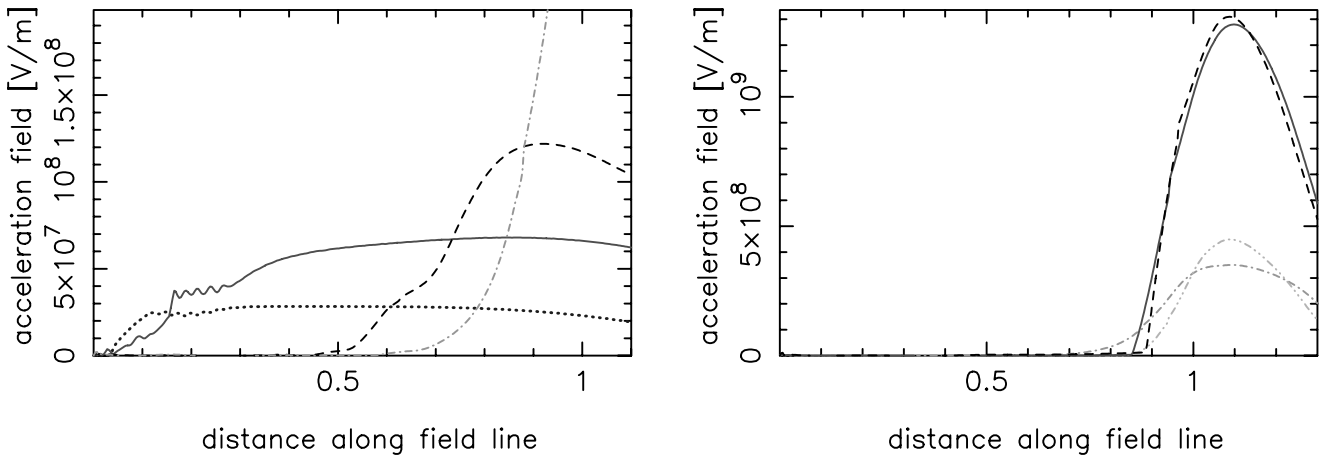


FIG. 9.—Same as Fig. 6, but with $\mu = 6.0 \times 10^{30}$ G cm^3; in the left panel, the dotted and solid curves correspond to $h = 0.039$ and 0.041, respectively. For the two other curves in the left panel and the four curves in the right panel, h takes the same values as in Fig. 6. [*See the electronic edition of the Journal for a color version of this figure.*]

how the solution changes if we adopt different values of kT_s, μ, and $\alpha_{\rm inc}$.

3.4. *Dependence on Surface Temperature*

In the same manner as in § 3.3, we calculate $E_\parallel(s, h = h_m/2)$ for $kT_s = 150$ eV and find that their distribution is similar to the $kT_s = 100$ eV case (i.e., Fig. 6). For example, sub/super-GJ current solutions are discriminated by the condition whether h_m is greater than 0.048 or not, and the maximum of $E_\parallel$ is 7.2×10^8 V m^{-1} for $0.20 < h_m < 0.24$. Other quantities, such as the particle and γ-ray distribution functions, are also similar. Therefore, we can conclude that the solution is little subject to change for the variation of kT_s, even though the photon-photon pair production rate increases with increasing kT_s. This is due to the negative feedback effect, which is discussed in § 4.2.

3.5. *Dependence on Magnetic Moment*

Let us examine how the solution depends on the magnetic moment, μ. In Figure 9, we present $E_\parallel(s, h = h_m/2)$ for seven discrete h_m values with $\mu = 6.0 \times 10^{30}$ G cm^3; in the left panel, the dotted and solid curves correspond to $h = 0.039$ and 0.041, respectively, instead of $h = 0.047$ and 0.048 as in Figure 6. It follows that the exerted $E_\parallel$ is greater than the case of $\mu = 4.0 \times 10^{30}$ G cm^3 (Fig. 6), because $\rho_{\rm GJ}$ increases 1.5 times. The negative feedback effect cannot cancel the increase of μ, unlike the increase of kT_s, because the right-hand side of equation (19) is more directly affected by the variation of μ through $\rho_{\rm GJ}$ than by the variation of kT_s through pair creation.

We also present the γ-ray spectrum for three different values of μ in Figure 10. It follows that both the peak energy and the flux of curvature γ-rays (around GeV energies) increase with increasing μ. This is because $\rho_{\rm GJ}$, and hence $E_\parallel$, increases with μ. It also follows that the secondary synchrotron flux (below 100 MeV) increases with μ, because the magnetic field strength increases in the magnetosphere. We find that a larger magnetic dipole moment, $\mu \geq 6 \times 10^{30}$ G cm^3, is preferable to explain the observed pulsed flux from the Crab pulsar.

If we adopt $\mu = 8 \times 10^{30}$ G cm^3, which is about twice as large as the dipole deduced value, the spectral shape becomes more consistent compared with smaller μ cases. We should note here that the moment of inertia, I, has to be large in this case. For example, if we assume a pure magnetic dipole radiation, the spin-down luminosity becomes $L_{\rm SD} = (2 \sin^2\alpha_{\rm inc}/3)(\mu^2\Omega^4/c^3) = 1.7 \times 10^{39}$ ergs s^{-1} for $\alpha_{\rm inc} = 70^\circ$. Equating $-\dot{E} = -I\Omega\dot{\Omega}$ with this $L_{\rm SD}$, we obtain $I = 3.9 \times 10^{45}$ g cm^2, which is consistent with the limit ($I > 3.04 \times 10^{45}$ g cm^2) derived from the consideration of energetics of the Crab nebula (Bejger & Haensel 2002). However, solving the time-dependent equations of force-free electrodynamics, Spitkovsky (2006) derived $L_{\rm SD} \approx (1 + \sin^2\alpha_{\rm inc}) \times (\mu^2\Omega^4/c^3)$, which gives $\approx 5.6 \times 10^{39}$ ergs s^{-1} for $\alpha_{\rm inc} = 70^\circ$. This large spin-down luminosity results in $I \approx 1.2 \times 10^{46}$ g cm^2, which is too large even compared with those obtained for a stiff

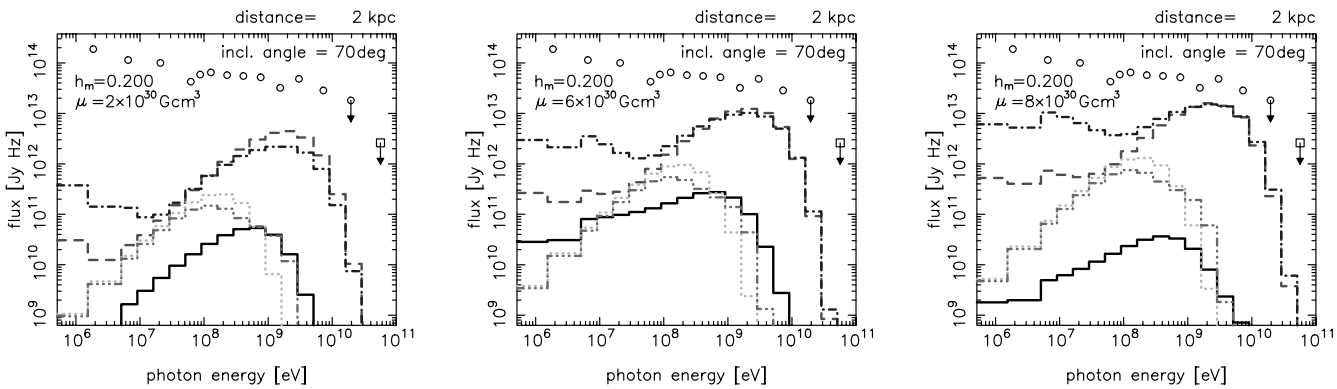


FIG. 10.—Same as Fig. 8 for $\alpha_{\rm inc} = 70^\circ$, $kT_s = 100$ eV, and $h_m = 0.200$, but with a different dipole moment, μ. [*See the electronic edition of the Journal for a color version of this figure.*]

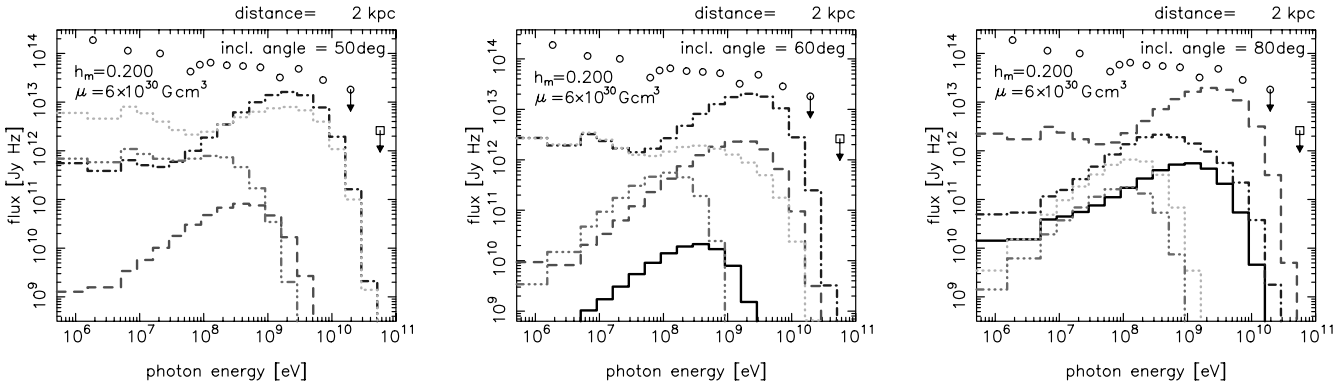


FIG. 11.—Same as Fig. 8 for $kT_s = 100$ eV, $\mu = 6.0 \times 10^{30}$ G cm^3, and $h_m = 0.200$, but with different magnetic inclination angle, $\alpha_{\rm inc}$. [*See the electronic edition of the Journal for a color version of this figure*.]

equation of state (Serot 1979a, 1979b; Pandharipande & Smith 1975). Thus, it implies either that μ should be less than 8×10^{30} G cm^3 or that the deduced magnetospheric current is too large when the relationship $L_{\rm SD} \approx (1 + \sin^2\alpha_{\rm inc})(\mu^2\Omega^4/c^3)$ is derived (for a discussion of the magnetospheric current determination, see § 4 of Hirotani 2006).

3.6. *Dependence on Magnetic Inclination*

Let us examine how the solution depends on the magnetic inclination angle, $\alpha_{\rm inc}$. Figure 11 shows the γ-ray spectra for $\mu = 6 \times 10^{30}$ G cm^3, $kT_s = 100$ eV, and $h_m = 0.200$, with three different inclination, $\alpha_{\rm inc} = 50^\circ$, 60°, and 80°, in the same manner as in Figure 8. The flux is averaged over the meridional emission angles between 44° and 58° (*solid line*), 58° and 72° (*dashed line*), 72° and 86° (*dash-dotted line*), 86° and 100° (*dotted line*), and 100° and 114° (*dash–triple-dotted line*) from the magnetic axis on the plane in which both the rotational and magnetic axes reside. We find that the γ-ray flux reaches a peak of $\sim 2 \times 10^{13}$ Jy Hz around 2 GeV and that this peak does not strongly depend on $\alpha_{\rm inc}$. This is because the pair creation efficiency, which governs the gap electrodynamics, crucially depends on the distance from the star, which has a small dependence on $\alpha_{\rm inc}$. However, we also find that the flux tends to be emitted into larger meridional angles from the magnetic axis (i.e., from outer regions) for smaller $\alpha_{\rm inc}$. The reasons are fourfold:

1. $\rho_{\rm GJ}$ decreases with decreasing $\alpha_{\rm inc}$ at a fixed s; as a result, the null surface appears at larger s for smaller $\alpha_{\rm inc}$.
2. $\rho_{\rm GJ}(s) = -\rho_{\rm GJ}(0)$ is realized at larger s for smaller $\alpha_{\rm inc}$.
3. In the region where $\rho_{\rm GJ} < -\rho_{\rm GJ}(0)$ holds, $E_\parallel$ is substantially screened by the discharge of created pairs. (Compare Fig. 5 and the right panel of Fig. 4.)
4. The unscreened $E_\parallel$ tends to appear at larger s for smaller $\alpha_{\rm inc}$, resulting in a γ-ray emission which concentrate in larger meridional angles.

We can alternatively interpret the explanation above as follows:

a) $|\rho_{\rm GJ}(0)|$ increases with decreasing $\alpha_{\rm inc}$.
b) The created current density, j_e, which is greater than $c|\rho_{\rm GJ}(0)|$ for a super-GJ solution, increases with decreasing $\alpha_{\rm inc}$. For example, we obtain $j_e = 0.62$, 0.67, 0.74, and 0.77 for $\alpha_{\rm inc} = 80^\circ$, 70°, 60°, and 50°, respectively, at $h = h_m/2 = 0.100$ with $\mu = 6 \times 10^{30}$ G cm^3 and $kT_s = 100$ eV.
c) A larger j_e results in a larger injection of the discharged positrons and the emitted ions into the strong-$E_\parallel$ region from the stellar side.
d) A larger injection of positive charges from the stellar side shifts the gap outward by the mechanism discussed in § 2 of Hirotani & Shibata (2001a).

For a smaller inclination, $\alpha_{\rm inc} \le 40^\circ$, the gap is located in $\varpi > 0.9\varpi_{\rm LC}$; that is, no super-GJ solution exists. Therefore, the observed γ-ray flux cannot be explained by the present theory, if the magnetic inclination is constrained to be less than 40° by some other methods.

3.7. *Particle Distribution Functions*

Let us examine how the particle distribution function evolves at different positions. Figure 12 represents the evolution of positronic distribution function from $s = 0.85\varpi_{\rm LC}$ (*dashed curve*), $0.90\varpi_{\rm LC}$ (*dash-dotted curve*), $0.95\varpi_{\rm LC}$ (*dash–triple-dotted curve*), $1.00\varpi_{\rm LC}$ (*solid curve*), to $1.30\varpi_{\rm LC}$ (*dotted curve*). It shows that the positrons are injected into the strong-$E_\parallel$ region ($s > 0.85\varpi_{\rm LC}$) with energies $10^4 < \Gamma < 3 \times 10^6$ because of the acceleration by the small-amplitude, residual $E_\parallel$ in $s < 0.85\varpi_{\rm LC}$ (Fig. 9, *right panel, solid curve*). The positrons are accelerated outward to attain $\Gamma \sim 4 \times 10^7$ at $s \sim 1.0\varpi_{\rm LC}$. They are subsequently decelerated by curvature cooling in $\varpi > 0.9\varpi_{\rm LC}$ (or equivalently $s > 1.1\varpi_{\rm LC}$ for $\alpha_{\rm inc} = 70^\circ$), where we artificially put

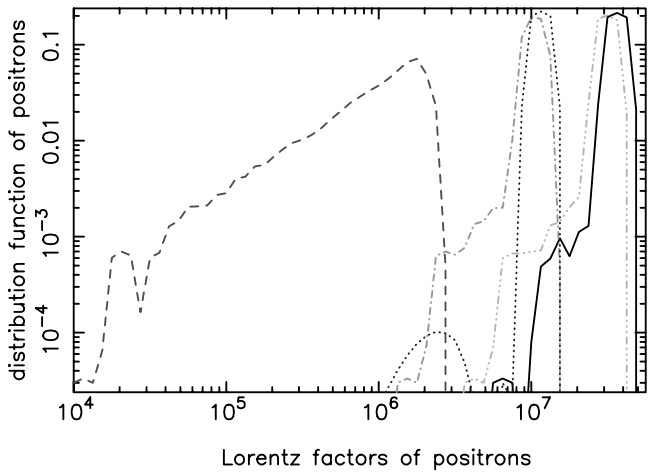


FIG. 12.—Energy spectrum of positrons at $s = 0.85\varpi_{\rm LC}$ (*dashed curve*), $0.90\varpi_{\rm LC}$ (*dash-dotted curve*), $0.95\varpi_{\rm LC}$ (*dash–triple-dotted curve*), $1.00\varpi_{\rm LC}$ (*solid curve*), and $1.30\varpi_{\rm LC}$ (*dotted curve*), for $\alpha_{\rm inc} = 70^\circ$, $\mu = 6.0 \times 10^{30}$ G cm^3, $kT_s = 100$ eV, and $h_m = 0.20$. [*See the electronic edition of the Journal for a color version of this figure*.]

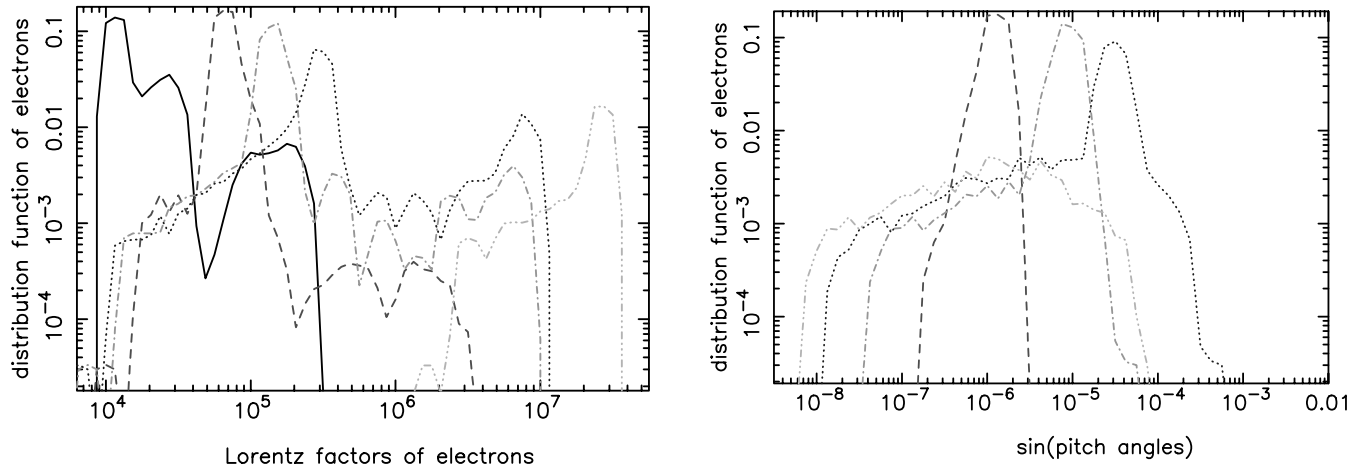


FIG. 13.—Distribution function of electrons at $s = 0.9\varpi_{\rm LC}$ (*dash–triple-dotted curves*), $0.4\varpi_{\rm LC}$ (*dotted curves*), $0.2\varpi_{\rm LC}$ (*dash-dotted curves*), $0.08\varpi_{\rm LC}$ (*dashed curves*), and 0 (*solid curves*), for $\alpha_{\rm inc} = 70^\circ$, $\mu = 6.0 \times 10^{30}$ G cm^3, $kT_s = 100$ eV, and $h_m = 0.20$. Left panel shows the Lorentz factor dependence, while the right one shows the pitch-angle dependence. [*See the electronic edition of the Journal for a color version of this figure.*]

$E_\parallel = 0$, to escape outward with $\Gamma \sim 10^7$ at $s \sim 1.3\varpi_{\rm LC}$. There is a small population of the positrons that have upscattered surface X-rays to possess smaller energies than the curvature-limited positrons. For example, within the gap ($s < 1.1\varpi_{\rm LC}$), the dash-dotted, dash–triple-dotted, and solid curves have the broad, lower-energy component, which connects with the curvature-limited peak component. However, in $s > 1.1\varpi_{\rm LC}$, we artificially put $E_\parallel = 0$; as a result, the positrons that have lost energies by ICS cannot be reaccelerated, forming a separate component in $\Gamma < 4 \times 10^6$ from the curvature-limited peak component, as the dotted curve shows. The upscattered photons obtain several TeV energies; however, they are totally absorbed by the strong magnetospheric infrared radiation field. Therefore, we depict only the photon energies below 100 GeV in Figures 8, 10, and 11.

Since most of the pairs are created inward, positrons return to migrate outward by the small-amplitude $E_\parallel$ in $s < 0.85\varpi_{\rm LC}$ (for $\mu = 6.0 \times 10^{30}$ G cm^3 and $\alpha_{\rm inc} = 70^\circ$), losing significant transverse momenta via synchrotron process to fall onto the ground-state Landau level in the strong-B region. Thus, their emission in the strong-$E_\parallel$ region is given by a pure-curvature formula.

Next, we consider the distribution function of electrons. In Figure 13 we present their evolution along the field line $h = h_m/2 = 0.100$ from $s = 0.90\varpi_{\rm LC}$ (*dash–triple-dotted curve*), $0.40\varpi_{\rm LC}$ (*dotted curve*), $0.20\varpi_{\rm LC}$ (*dash-dotted curve*), $0.08\varpi_{\rm LC}$ (*dashed curve*), to 0 (*solid curve*). Left panel shows the energy spectrum. Electrons created in $s < 0.85\varpi_{\rm LC}$ cannot be accelerated by $E_\parallel$ efficiently; thus, their energy spectrum becomes broad, as the dotted, dash-dotted, and dashed curves indicate (i.e., particle Lorentz factors do not concentrate at the curvature-limited terminal value). From $s = 0.08\varpi_{\rm LC}$ to 0, electrons are decelerated via synchrocurvature radiation and nonresonant IC scatterings. Finally, they hit the stellar surface with $\Gamma < 3 \times 10^5$. Assuming that the azimuthal gap width is π radians, we obtain $L_{\rm PC} = 2.6 \times 10^{31}$ ergs s^{-1} as the heated polar-cap luminosity. Thus, the X-ray emission due to the bombardment is negligible, compared with the total soft X-ray luminosity (0.1–2.4 keV) of 7.6×10^{34} ergs s^{-1}($\Delta\Omega_{\rm X}$/sr) (e.g., Becker & Trümper 1997), where $\Delta\Omega_{\rm X}$ refers to the emission solid angle.

Let us see the pitch-angle evolution of the electrons, which is presented in the right panel of Figure 13. In the outer part of the gap, the electrons are created by the collisions between the outward-directed γ-rays and the surface X-rays. Thus, created electrons have outward momenta initially, then return by the positive $E_\parallel$, losing their perpendicular momentum substantially via synchrotron radiation. Thus, at $s = 0.90\varpi_{\rm LC}$, the dash–triple-dotted curve shows that their pitch angles, χ, are less than 8×10^{-5}. However, most of the pairs are created by the inward-directed γ-rays in $s < 0.6\varpi_{\rm LC}$; thus, electrons have initial inward momenta to migrate inward by the small-amplitude, residual $E_\parallel$. Since such inward-created electrons do not change their migration direction, their pitch angles are greater than those of the outward-created ones, as the dotted curve demonstrates. As the electrons migrate inward, they lose perpendicular momenta via synchrocurvature radiation in the strong B-field, reducing their pitch angles, as the dotted, dash-dotted, and dashed curves indicate.

We should point out that a pure curvature formula cannot be applied to the electrons. For example, at $s = 0.4\varpi_{\rm LC}$, the dotted curve in Figure 13 demonstrates that electrons have $10^4 < \Gamma < 10^7$ and $10^{-8} < \sin\chi < 10^{-3.5}$. Noting that we have $B = 3.0 \times 10^7$ G at $s = 0.4\varpi_{\rm LC}$, we find that newly created electrons, which have lower energies ($\Gamma < 10^6$) and larger pitch angles ($\sin\chi > 10^{-5}$), emit synchrocurvature radiation, rather than pure-curvature radiation, as Figure 14 shows. At $s = 0.2\varpi_{\rm LC}$, we have $B = 3.6 \times 10^8$ G; thus, the dash-dotted curve shows that the pure-curvature formula is totally inapplicable as we consider a smaller distance from the star. The only exception is the innermost region ($s < 5r_* = 0.031\varpi_{\rm LC}$ and $B > 5 \times 10^{10}$ G), where electrons suffer substantial de-excitation via synchrotron radiation, falling at last onto the ground-state Landau level. In this region, electrons emit via pure curvature radiation. We thus artificially assume $\sin\chi = 10^{-20}$, which guarantees pure curvature emission, and do not depict the solid curve in the right panel of Figure 13. Since pair creation and the resulting screening of $E_\parallel$ is governed by the inward-directed γ-ray flux and spectrum, it is essential to adopt the correct radiation formula by computing the pitch-angle evolution of inward-migrating particles.

3.8. *Formation of Magnetically Dominated Wind*

Let us finally consider the magnetic dominance within the light cylinder. First, we introduce the magnetization parameter,

$$\sigma \equiv \frac{B^2}{4\pi}\left[\Gamma m_e c^2 \iiint (N_+ + N_-) d^3\boldsymbol{p} + \Gamma_{\rm ion} m_{\rm ion} c^2 \iiint N_{\rm ion} d^3\boldsymbol{p}\right]^{-1} = \frac{e(B/2)\varpi_{\rm LC}}{j_e \Gamma m_e c^2 + j_{\rm ion}\Gamma_{\rm ion} m_{\rm ion} c^2}, \quad (69)$$

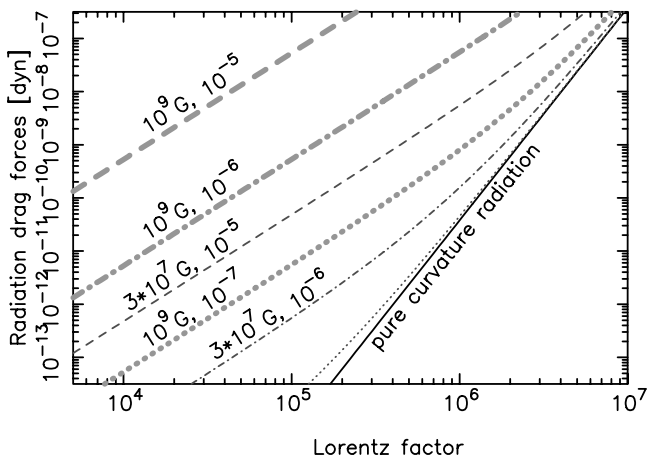


FIG. 14.—Pure-curvature (*solid curve*) vs. synchrocurvature radiation-reaction forces. For the latter, we adopt the pitch angles $\chi = 10^{-5}$, 10^{-6}, and 10^{-7} rad for the dashed, dash-dotted, and dotted curves, respectively, and $B = 3 \times 10^7$ and 10^9 G for the thin and thick curves, respectively. Curvature radius is assumed to be $0.4\varpi_{\rm LC} = 6.37 \times 10^7$ cm. [*See the electronic edition of the Journal for a color version of this figure*.]

where $N_{\rm ion}$ and $\Gamma_{\rm ion}$ refer to the distribution function and the averaged Lorentz factor of the ions, respectively. Evaluating equation (69) at the light cylinder, and noting $\Gamma_{\rm ion} m_{\rm ion} c^2 = |e\Delta\Psi_{\rm gap}|$, where $|e\Delta\Psi_{\rm gap}| \approx (B/4)h_m^2\varpi_{\rm LC}$ refers to the potential drop in the gap (see eq. [68]), we obtain

$$\sigma_{\rm LC} \approx \frac{1}{h_m^2}\frac{2}{j_e \Gamma m_e c^2/|e\Delta\Psi_{\rm gap}| + j_{\rm ion}}. \quad (70)$$

Recalling $j_{\rm ion} < j_e < 1$, $\Gamma m_e c^2 < |e\Delta\Psi_{\rm gap}|$, and $h_m < 1$, we can conclude that the magnetic energy flux is always greater than the particle kinetic energy flux at the light cylinder, regardless of the species of the accelerated particles, of the sign of $E_\parallel$, or of the gap position (i.e., whether inner or outer magnetosphere). Only when the gap is formed along most of the open field lines (i.e., $h_m \sim 1$), $\sigma_{\rm LC}$ can be of the order of unity. Since the second factor in equation (70) does not change significantly for different values of parameters except for h_m, $\sigma_{\rm LC}$ solely depends on h_m. Substituting $j_{\rm ion} \sim 0.3$, $j_e \sim 0.6$, $\Gamma m_e c^2/|e\Delta\Psi_{\rm gap}| \sim 0.25$ in $(3/16)h_m \le h \le (13/16)h_m$ for $\alpha_{\rm inc} = 70^\circ$, $\mu = 6 \times 10^{30}$ G cm^3, and $h_m = 0.20$, we obtain $\sigma_{\rm LC} \sim 110$.

In short, along the open field lines threading the gap, Poynting flux dominates particle kinetic energy flux by a factor of 100 at the light cylinder. Positrons escape from the gap with $\Gamma \sim 10^7$, while ions escape with $\Gamma_{\rm ion} \sim 10^4$.

4. SUMMARY AND DISCUSSION

To conclude, we investigated the self-consistent electrodynamic structure of a particle accelerator in the Crab pulsar magnetosphere on the two-dimensional surface that contains the magnetic field lines threading the stellar surface on the plane in which both the rotation and magnetic axes reside. We regard the transfield thickness, h_m, of the gap as a free parameter, instead of trying to constrain it. For a small h_m, the created current density, j_e, becomes sub-Goldreich-Julian (sub-GJ), giving the traditional outer-gap solution but with negligible γ-ray flux. However, as h_m increases, j_e increases to become super-GJ, giving a new gap solution with substantially screened acceleration electric field, $E_\parallel$, in the inner part. In this case, the gap extends toward the neutron star with a small-amplitude positive $E_\parallel$, which extracts ions from the stellar surface. It is essential to examine the pitch-angle evolution of the created particles, because the inward-migrating particles emit γ-rays, which govern the gap electrodynamics through pair creation, via a synchrocurvature process rather than a pure-curvature one. The resulting spectral shape of the outward-directed γ-rays is consistent with the existing observations; however, their predicted fluxes appear insufficient. The pulsar wind at the light cylinder is magnetically dominated: along the field lines threading the gap, the magnetization parameter, $\sigma_{\rm LC}$, is about 10^2.

4.1. *How to Obtain Sufficient γ-Ray Flux*

The obtained γ-ray fluxes in the present work are all below the observed values. Nevertheless, this problem may be solved if we extend the current analysis into a three-dimensional configuration space. As mentioned in § 2.4, we assume $k_\varphi = 0$ and neglect the aberration of photon emission directions. However, in a realistic three-dimensional pulsar magnetosphere, γ-rays will have angular momenta and may be emitted in a limited solid angle as suggested by the caustic model (e.g., Dyks & Rudak 2003; Dyks et al. 2004), which incorporates the effect of aberration of photons and that of time-of-flight delays. In particular, in the trailing peak of a highly inclined rotator, photons emitted at different altitudes s will be beamed in a narrow solid angle to be piled up at the same phase of a pulse (Morini 1983; Romani & Yadigaroglu 1995), resulting in a γ-ray flux that is an order of magnitude greater than the present values. Thus, the insufficient γ-ray fluxes do not suggest the inapplicability of the present method. It is noteworthy that the meridional propagation angles of the emitted photons (e.g., different curves in Figs. 8, 10, and 11) can be readily translated into the emissivity distribution in the gap as a function of s. Therefore, in this work, we do not sum up the γ-ray fluxes emitted into different meridional angles taking account of the aberration of light.

4.2. *Stability of the Gap*

Let us discuss the electrodynamic stability of the gap, by considering whether an initial perturbation of some quantity tends to be canceled or not. In the present paper, we consider that the soft photon field is given and unchanged when gap quantities vary. Thus, let us first consider the case in which the soft photon field is fixed. Imagine that the number of created pairs is decreased as an initial perturbation. It leads to an increase of the potential drop due to less efficient screening by the discharged pairs, and hence to an increase of particle energies. Then the particles emit synchrocurvature radiation efficiently, resulting in an increase of the created pairs, which tends to cancel the initial decrease of created pairs.

Let us next consider the case in which the soft photon field also changes. Imagine again that the created pairs are decreased as an initial perturbation. It leads to an increase of particle energies in the same manner as discussed just above. The increased particle energies increase not only the number and density of synchrocurvature γ-rays, but also the surface blackbody emission from heated polar caps and the secondary magnetospheric X-rays. Even though neither the heated polar-cap emission nor the magnetospheric emission is taken into account as the soft photon field illuminating the gap in this paper, they all work, in general, to increase the pair creation within the gap, which cancels the initial decrease of created pairs more strongly than for the case of the fixed soft photon field.

Because of such negative feedback effects, solutions exist in a wide parameter space. For example, the created current density is almost unchanged for a wide range of h_m (e.g., compare the dash-dotted and dash–triple-dotted curves in Fig. 7). On these grounds,

although the perturbation equations are not solved under appropriate boundary conditions for the perturbed quantities, we conjecture that the particle accelerator is electrodynamically stable, irrespective whether the X-ray field illuminating the gap is thermal or nonthermal origin.

4.3. *Local versus Global Currents*

Let us briefly look at the relationship between the locally determined current density $j_{\rm gap}$ (eq. [43]) and the globally required one, $j_{\rm global}$. It is possible that $j_{\rm global}$ is constrained independently from the gap electrodynamics by the dissipation at large distances (Shibata 1997), which provides the electric load in the current circuit, or by the condition that the magnetic flux function should be continuous across the light cylinder, as discussed in the recent force-free argument of the transfield equation (Contopoulos et al. 1999; Goodwin et al. 2004; Gruzinov 2005; Spitkovsky 2006). In either case, $j_{\rm global}$ will be more or less close to unity (i.e., typical GJ value). On the other hand, as demonstrated in § 3.3, for super-GJ cases, $j_{\rm gap}$ is automatically regulated around 0.9 for a wide parameter range. Thus, the discrepancy between $j_{\rm gap}$ and $j_{\rm global}$ is small provided that h_m is large enough to maintain the created current density at a super-GJ value. The small imbalance $j_{\rm global} - j_{\rm gap}$ may have to be compensated by a current injection across the outer boundary (if the gap terminates inside of the light cylinder, charged particles could be injected from the outer boundary), or by an additional ionic emission from the stellar surface (if the imbalance leads to an additional residual $E_\parallel$ at the surface). In any case, the injected current is small compared with $j_{\rm gap}$; thus, it will not change the electrodynamics significantly, even though the gap active region may be shifted to some degree along the magnetic field lines, as demonstrated by Hirotani & Shibata (2001a, 2001b, 2002), TSH04, and TSHC06.

4.4. *Created Pairs in the Inner Magnetosphere*

Let us devote a little more space to examining the particle flux along the open field lines that do *not* thread the gap (i.e., $h_m < h < 1$). Since $E_\parallel$ vanishes, the created, secondary pairs emit synchrotron photons, which are capable of cascading into tertiary and higher generation pairs by γ-γ or γ-$\boldsymbol{B}$ collisions. Examining the cascade, we can calculate the rate of pair creation, which takes place mainly in the inner magnetosphere. Denoting that the pair creation rate is $\kappa_w(h)(\Omega B/2\pi e)$ per unit area per second, we find $\kappa_w = 2.2\times10^4$, 2.1×10^4, 1.9×10^4, 1.8×10^4, 1.6×10^4, 1.1×10^4, 1.0×10^4, 0.99×10^4, 0.95×10^4, 0.96×10^4, and 1.0×10^4 at $h = 0.20125$, 0.2025, 0.20375, 0.205, 0.305, 0.405, 0.505, 0.605, 0.705, 0.805, and 0.905, respectively, for $\alpha_{\rm inc} = 70^\circ$, $\mu = 6.0\times10^{30}$ G cm^3, and $h_m = 0.200$. Thus, the averaged creation rate becomes $\bar\kappa_w = 1.4\times10^4(\Omega B/2\pi e)$ pairs per unit area per second, giving $\dot N_{\rm pair} = 3.8\times10^{38}$ s^{-1} as the pair creation rate in the entire magnetosphere. It should be noted that this $\dot N_{\rm pair}$ appears less than the constraints that arise from consideration of magnetic dissipation in the wind zone (Kirk & Lyubarsky 2003, who derived 10^{40} s^{-1}), and of Crab Nebula's radio synchrotron emission (Arons 2004, who derived $10^{40.5}$ s^{-1}).

Due to strong synchrotron radiation, these inwardly created particles quickly lose energy to fall onto the lowest Landau level, preserving longitudinal momentum $\sim m_e c$ per particle. These nonrelativistic particles possess momentum flux of $2\dot N_{\rm pair} m_e c/(\pi R_{\rm PC}^2) \sim 1.0\times10^{12}$ dyn cm^{-2}, where $R_{\rm PC} \sim (r_*^3/\varpi_{\rm LC})^{1/2}$ denotes the polar cap radius. On the other hand, the surface X-ray field has the upward momentum flux of $6.0\times10^8(kT/100\ {\rm eV})^4$ dyn cm^{-2}. Thus, the created pairs will not be pushed back by resonant scatterings. They simply fall onto the stellar surface with nonrelativistic velocities. The luminosity of the e^--e^+ annihilation line is about 3×10^{26} ergs s^{-1}, which is negligible (e.g., compared with the γ-ray luminosity $\sim10^{34.5}$ ergs s^{-1}). On these grounds, for the Crab pulsar, we must conclude that the present work fails to explain the injection rate of the wind particles, in the same way as in other outer-gap models.

4.5. *Comparison with Polar-Slot Gap Model*

It is worth comparing the present results with the polar-slot-gap model proposed by MH03, MH04a, and MH04b, who obtained a quite different solution (e.g., negative $E_\parallel$ in the gap) solving essentially the same equations under analogous boundary conditions for the same pulsar as in the present work. The only difference is the transfield thickness of the gap. Estimating the transfield thickness to be $\Delta l_{\rm SG} \sim h_m r_* (r/\varpi_{\rm LC})^{1/2}$, which is a few hundred times thinner than the present work, they extended the solution (near the polar cap surface) that was obtained by MT92 into the higher altitudes (toward the light cylinder). Because of this very small $\Delta l_{\rm SG}$, emitted γ-rays do not efficiently materialize within the gap; as a result, the created and returned positrons from the higher altitudes do not break down the original assumption of the completely charge-separated SCLF near the stellar surface.

To avoid the reversal of $E_\parallel$ in the gap (from negative near the star to positive in the outer magnetosphere), or equivalently, to avoid the reversal of the sign of the effective charge density, $\rho_{\rm eff} = \rho - \rho_{\rm GJ}$, along the field line, MH04a and MH04b assumed that $\rho_{\rm eff}/B$ nearly vanishes and remains constant above a certain altitude, $s = s_c$, where s_c is estimated to be within a few neutron star radii. Because of this assumption, $E_\parallel$ is suppressed at a very small value and the pair creation becomes negligible in the entire gap. In another word, the enhanced screening is caused not only by the proximity of two conducting boundaries, but also by the assumption of $\partial(\rho_{\rm eff}/B)/\partial s = 0$ within the gap (see eq. [68]). To justify this ρ/B distribution, MH04a and MH04b proposed an idea that ρ should grow by the *cross-field motion* of charges due to the toroidal forces, and that $\rho_{\rm eff}/B$ is a small constant so that $c\rho_{\rm eff}/B$ may not exceed the flux of the emitted charges from the star, which ensures the *equipotentiality* of the slot-gap boundaries (see § 2.2 of MH04a for details).

The cross-field motion becomes important if particles gain angular momenta as they migrate outward to pick up energies that are a nonnegligible fraction of the difference of the cross-field potential between the two conducting boundaries. Denoting the fraction as ϵ, we obtain $\Gamma m_e c^2 \dot\varphi \Omega (\varpi/c)^2 = \epsilon e B \Delta l_{\rm SG}$ (Mestel et al. 1985; eq. [12] of MH04a). If we substitute their estimate $\Delta l_{\rm SG} \sim r_*/20$, we obtain $\epsilon \sim 0.33(\dot\varphi/\Omega)\gamma_7 B_6^{-1} r_6^{-3}(\varpi/\varpi_{\rm LC})^2$, where $\gamma_7 = \Gamma/10^7$, $B_6 = B_*/10^6$ G, and $r_6 = r_*/10$ km; therefore, the cross-field motion becomes important in the outer magnetosphere within their slot-gap model. A larger value of $\Delta l_{\rm SG}$ is incompatible with the constancy of $\rho_{\rm eff}/B$ due to the cross-field motion in the higher altitudes.

As for the equipotentiality of the boundaries, it seems reasonable to suppose that $c|\rho_{\rm eff}|/B < c|\rho_*|/B_*$ should be held at any altitudes in the gap, as MH04a suggested, where ρ_* denotes the real charge density in the vicinity of the stellar surface. However, the assumption that $\rho_{\rm eff}/B$ is a small positive constant may be too strong, because it is only a sufficient condition of $c|\rho_{\rm eff}|/B < c|\rho_*|/B_*$.

In the present paper, on the other hand, we assume that the magnetic fluxes threading the gap are unchanged, considering that charges freely move along the field lines on the upper (and lower) boundaries. As a result, the gap becomes much thicker than in MH04a and MH04b; namely, $\Delta l_{\rm SG} \sim 0.5 h_m \varpi_{\rm LC}$, which gives $\epsilon < 10^{-3}$. Therefore, we can neglect the cross-field motion and justify the constancy of ρ/B in the outer region of the gap, where

pair creation is negligible. In the inner magnetosphere, $\rho_{\rm eff}/B$ becomes approximately a negative constant, owing to the discharge of the copiously created pairs. Because of this negativity of $\rho_{\rm eff}/B$, a positive $E_\parallel$ is exerted. For a super-GJ solution, we obtain $j_e + \ j_{\rm ion} \sim 0.9 > \rho_{\rm eff}/(\Omega B/2\pi)$, which guarantees the equipotentiality of the boundaries. For a sub-GJ solution, a problem may occur regarding the equipotentiality; nevertheless, we are not interested in this kind of solutions.

In short, whether the gap solution becomes MH04a-like (with a negative $E_\parallel$ as an outward extension of the polar-cap model) or like the model in the present paper (with a positive $E_\parallel$ as an inward extension of the outer-gap model) entirely depends on the transfield thickness and on the resulting $\rho_{\rm eff}/B$ variation along the field lines. If $\Delta l_{\rm SG} \sim r_*/10$ holds in the outer magnetosphere, $\rho_{\rm eff}/B$ could be a small positive constant by the cross-field motion of charges (without pair creation); in this case, the current is slightly sub-GJ with electron emission from the neutron star surface, as MH04a, MH04b suggested. On the other hand, if $\Delta l_{\rm SG} > \varpi_{\rm LC}/40$ holds in the outer magnetosphere, $\rho_{\rm eff}/B$ takes a small negative value by the discharge of the created pairs (see Fig. 5); in this case, the current is super-GJ with ion emission from the surface, as demonstrated in the present paper. Since no studies have ever successfully constrained the gap transfield thickness, there is room for further investigation on this issue.

The author is grateful to J. G. Kirk, B. Rudak, S. Shibata, K. S. Cheng, A. K. Harding, J. Arons, R. Taam, H. K. Chang, and J. Takata for helpful suggestions. Some important parts of this work were prepared while the author studied at Max-Planck-Institut für Kernphysik, Heidelberg. This work is supported by the Theoretical Institute for Advanced Research in Astrophysics (TIARA) operated under Academia Sinica and the National Science Council Excellence Projects program in Taiwan administered through grant NSC 94-2752-M-007-001. Also, this work is partly supported by KBN through grant 2P03D.004.24 to B. Rudak, which enabled the author to use the MEDUSA cluster at CAMK Toruń. The final computations were carried out with the aid of the Blade Tank servers at TIARA, Taipei.

APPENDIX

Explicit expressions of equations (20) and (21) are as follows:

$$g^{ss} = g^{rr}\left(\frac{\partial s}{\partial r}\right)^2_{\theta,\varphi} + g^{\theta\theta}\left(\frac{\partial s}{\partial \theta}\right)^2_{\varphi,r} - \frac{k_0}{\rho_w^2}\left(\frac{\partial s}{\partial \varphi}\right)^2_{r,\theta}, \tag{A1}$$

$$g^{\theta_*\theta_*} = g^{rr}\left(\frac{\partial \theta_*}{\partial r}\right)^2_{\theta,\varphi} + g^{\theta\theta}\left(\frac{\partial \theta_*}{\partial \theta}\right)^2_{\varphi,r} - \frac{k_0}{\rho_w^2}\left(\frac{\partial \theta_*}{\partial \varphi}\right)^2_{r,\theta}, \tag{A2}$$

$$g^{\varphi_*\varphi_*} = g^{rr}\left(\frac{\partial \varphi_*}{\partial r}\right)^2_{\theta,\varphi} + g^{\theta\theta}\left(\frac{\partial \varphi_*}{\partial \theta}\right)^2_{\varphi,r} - \frac{k_0}{\rho_w^2}\left(\frac{\partial \varphi_*}{\partial \varphi}\right)^2_{r,\theta}, \tag{A3}$$

$$g^{s\theta_*} = g^{rr}\left(\frac{\partial s}{\partial r}\right)_{\theta,\varphi}\left(\frac{\partial \theta_*}{\partial r}\right)_{\theta,\varphi} + g^{\theta\theta}\left(\frac{\partial s}{\partial \theta}\right)_{\varphi,r}\left(\frac{\partial \theta_*}{\partial \theta}\right)_{\varphi,r} - \frac{k_0}{\rho_w^2}\left(\frac{\partial s}{\partial \varphi}\right)_{r,\theta}\left(\frac{\partial \theta_*}{\partial \varphi}\right)_{r,\theta}, \tag{A4}$$

$$g^{\theta_*\varphi_*} = g^{rr}\left(\frac{\partial \theta_*}{\partial r}\right)_{\theta,\varphi}\left(\frac{\partial \varphi_*}{\partial r}\right)_{\theta,\varphi} + g^{\theta\theta}\left(\frac{\partial \theta_*}{\partial \theta}\right)_{\varphi,r}\left(\frac{\partial \varphi_*}{\partial \theta}\right)_{\varphi,r} - \frac{k_0}{\rho_w^2}\left(\frac{\partial \theta_*}{\partial \varphi}\right)_{r,\theta}\left(\frac{\partial \varphi_*}{\partial \varphi}\right)_{r,\theta}, \tag{A5}$$

$$g^{\varphi_* s} = g^{rr}\left(\frac{\partial \varphi_*}{\partial r}\right)_{\theta,\varphi}\left(\frac{\partial s}{\partial r}\right)_{\theta,\varphi} + g^{\theta\theta}\left(\frac{\partial \varphi_*}{\partial \theta}\right)_{\varphi,r}\left(\frac{\partial s}{\partial \theta}\right)_{\varphi,r} - \frac{k_0}{\rho_w^2}\left(\frac{\partial \varphi_*}{\partial \varphi}\right)_{r,\theta}\left(\frac{\partial s}{\partial \varphi}\right)_{r,\theta}, \tag{A6}$$

and

$$A^s \equiv \frac{c^2}{\sqrt{-g}}\left\{\partial_r\left[\frac{g_{\varphi\varphi}}{\rho_w^2}\sqrt{-g}g^{rr}\left(\frac{\partial s}{\partial r}\right)_{\theta,\varphi}\right] + \partial_\theta\left[\frac{g_{\varphi\varphi}}{\rho_w^2}\sqrt{-g}g^{\theta\theta}\left(\frac{\partial s}{\partial \theta}\right)_{\varphi,r}\right]\right\} - \frac{c^2 g_{\varphi\varphi}}{\rho_w^2}\frac{k_0}{\rho_w^2}\left(\frac{\partial^2 s}{\partial \varphi^2}\right)_{r,\theta}, \tag{A7}$$

$$A^{\theta_*} \equiv \frac{c^2}{\sqrt{-g}}\left\{\partial_r\left[\frac{g_{\varphi\varphi}}{\rho_w^2}\sqrt{-g}g^{rr}\left(\frac{\partial \theta_*}{\partial r}\right)_{\theta,\varphi}\right] + \partial_\theta\left[\frac{g_{\varphi\varphi}}{\rho_w^2}\sqrt{-g}g^{\theta\theta}\left(\frac{\partial \theta_*}{\partial \theta}\right)_{\varphi,r}\right]\right\} - \frac{c^2 g_{\varphi\varphi}}{\rho_w^2}\frac{k_0}{\rho_w^2}\left(\frac{\partial^2 \theta_*}{\partial \varphi^2}\right)_{r,\theta}, \tag{A8}$$

$$A^{\varphi_*} \equiv \frac{c^2}{\sqrt{-g}}\left\{\partial_r\left[\frac{g_{\varphi\varphi}}{\rho_w^2}\sqrt{-g}g^{rr}\left(\frac{\partial \varphi_*}{\partial r}\right)_{\theta,\varphi}\right] + \partial_\theta\left[\frac{g_{\varphi\varphi}}{\rho_w^2}\sqrt{-g}g^{\theta\theta}\left(\frac{\partial \varphi_*}{\partial \theta}\right)_{\varphi,r}\right]\right\} - \frac{c^2 g_{\varphi\varphi}}{\rho_w^2}\frac{k_0}{\rho_w^2}\left(\frac{\partial^2 \varphi_*}{\partial \varphi^2}\right)_{r,\theta}. \tag{A9}$$

REFERENCES

Arons, J. 1983, Nature, 302, 301
———. 2004, Adv. Space Res., 33, 466
Arons, J., & Scharlemann, E. T. 1979, ApJ, 231, 854
Becker, W., & Trümper, J. 1997, A&A, 326, 682
Bejger, M., & Haensel, P. 2002, A&A, 396, 917
Beskin, V. S., Istomin, Ya. N., & Par'ev, V. I. 1992, Soviet Astron., 36, 642
Camenzind, M. 1986a, A&A, 156, 137
———. 1986b, A&A, 162, 32
Cheng, K. S., Ho, C., & Ruderman, M. 1986a, ApJ, 300, 500 (CHR86a)
———. 1986b, ApJ, 300, 522 (CHR86b)
Cheng, K. S., Ruderman, M., & Zhang, L. 2000, ApJ, 537, 964 (CRZ00)
Cheng, K. S., & Zhang, L. 1996, ApJ, 463, 271

Chiang, J., & Romani, R. W. 1992, ApJ, 400, 629
———. 1994, ApJ, 436, 754
Contopoulos, I., Kazanas, D., & Fendt, C. 1999, ApJ, 511, 351
Daugherty, J. K., & Harding, A. K. 1982, ApJ, 252, 337
———. 1996, ApJ, 458, 278
de Naurois, M., et al. 2002, ApJ, 566, 343
Dermer, C. D., & Sturner, S. J. 1994, ApJ, 420, L75
Dyks, J., Harding, A. K., & Rudak, B. 2004, ApJ, 606, 1125
Dyks, J., & Rudak, B. 2003, ApJ, 598, 1201
Erber, T. 1966, Rev. Mod. Phys., 38, 626
Fierro, J. M., Michelson, P. F., Nolan, P. L., & Thompson, D. J. 1998, ApJ, 494, 734
Goldreich, P., & Julian, W. H. 1969, ApJ, 157, 869
Goodwin, S. P., Mestel, J., Mestel, L., & Wright, G. A. E. 2004, MNRAS, 349, 213
Gruzinov, A. 2005, Phys. Rev. Lett., 94, 021101
Harding, A. K., Tademaru, E., & Esposito, L. S. 1978, ApJ, 225, 226
Hirotani, K. 2006, Mod. Phys. Lett. A, 21, 1319
Hirotani, K., Harding, A. K., & Shibata, S. 2003, ApJ, 591, 334 (HHS03)
Hirotani, K., & Shibata, S. 1999a, MNRAS, 308, 54
———. 1999b, MNRAS, 308, 67
———. 1999c, PASJ, 51, 683
———. 2001a, MNRAS, 325, 1228
———. 2001b, ApJ, 558, 216
———. 2002, ApJ, 564, 369
Jackson, J. D. 1962, Classical Electrodynamics (New York: Wiley)
Jones, P. B. 1985, Phys. Rev. Lett., 55, 1338
Kanbach, G. 1999, Astrophys. Lett. Commun., 38, 17
Kirk, J., & Skjæraasen, O. 2003, ApJ, 591, 366
Kuiper, L., Hermsen, W., Cusumano, G., Riehl, R., Schönfelder, V., Strong, A., Bennett, K., & McConnell, M. L. 2001, A&A, 378, 918
Lense, J., & Thirring, H. 1918, Phys. Z., 19, 156 (English transl. in Gen. Relativ. Gravitation, 16, 711 [1984])
Mestel, L. 1971, Nature, 233, 149
Mestel, L., Robertson, J. A., Wang, Y. M., & Westfold, K. C. 1985, MNRAS, 217, 443
Morini, M. 1983, MNRAS, 202, 495
Muslimov, A. G., & Harding, A. K. 2003, ApJ, 588, 430 (MH03)
———. 2004a, ApJ, 606, 1143 (MH04a)
———. 2004b, ApJ, 617, 471 (MH04b)
———. 2005, ApJ, 630, 454
Muslimov, A. G., & Tsygan, A. I. 1992, MNRAS, 255, 61 (MT92)
Nakamura, T., & Yabe, T. 1990, Comput. Phys. Comm., 120, 122
Neuhauser, D., Koonin, S. E., & Langanke, K. 1987, Phys. Rev. A, 36, 4163
Neuhauser, D., Langanke, K., & Koonin, S. E. 1986, Phys. Rev. A, 33, 2084
Nolan, P. L., et al. 1993, ApJ, 409, 697
Pandharipande, V. R., & Smith, R. A. 1975, Nucl. Phys. A, 237, 507
Romani, R. W. 1996, ApJ, 470, 469
Romani, R. W., & Yadigaroglu, I. A. 1995, ApJ, 438, 314
Scharlemann, E. T., Arons, J., & Fawley, W. T. 1978, ApJ, 222, 297 (SAF78)
Serot, B. D. 1979a, Phys. Lett. B, 87, 172
———. 1979b, Phys. Lett. B, 87, 403
Shibata, S. 1997, MNRAS, 287, 262
Spitkovsky, A. 2006, ApJ, 648, L51
Sturner, S. J., Dermer, C. D., & Michel, F. C. 1995, ApJ, 445, 736
Takahashi, M., Nitta, S., Tatematsu, Y., & Tomimatsu, A. 1990, ApJ, 363, 206
Takata, J., Shibata, S., & Hirotani, K. 2004, MNRAS, 354, 1120 (TSH04)
Takata, J., Shibata, S., Hirotani, K., & Chang, H.-K. 2006, MNRAS, 366, 1310 (TSHC06)
Tennant, A. F., et al. 2001, ApJ, 554, L173
Thompson, D. J. 2001, in AIP Conf. Proc. 558, High Energy Gamma-Ray Astronomy, ed. A. Goldwurm et al. (New York: AIP), 103
Ulmer, M. P., et al. 1995, ApJ, 448, 356
Zhang, L., & Cheng, K. S. 1997, ApJ, 487, 370
Znajek, R. L. 1977, MNRAS, 179, 457